Target-agnostic discovery of Rett Syndrome therapeutics by coupling computational network analysis and CRISPR-enabled *in vivo* disease modeling

Novak, R.[1,†,*], Lin, T.[1,*], Kaushal, S.[1], Sperry, M.[1], Vigneault, F.[1,†], Gardner, E.[1,†], Loomba, S.[1], Shcherbina, K.[1], Keshari, V.[1], Dinis, A.[1], Vasan, A.[1], Chandrasekhar, V.[1], Takeda, T.[1], Turner, J.R. [2], Levin, M. [1,3], Ingber, D.E. [1,4,5,#]

[1] Wyss Institute for Biologically Inspired Engineering, Harvard University, Boston, MA, USA

[2] Laboratory of Mucosal Barrier Pathobiology, Department of Pathology, Brigham and Women's Hospital and Harvard Medical School, Boston, MA, USA

[3] Allen Discovery Center at Tufts University, Medford, MA, USA

[4] Harvard John A. Paulson School of Engineering and Applied Sciences, Harvard University, Cambridge, MA, USA

[5] Vascular Biology Program and Department of Surgery, Boston Children's Hospital and Harvard Medical School, Boston, MA, USA

[†]Present address: Unravel Biosciences, Inc., Boston, MA, USA

* Contributed equally to this manuscript

Corresponding author: Donald E. Ingber, MD, PhD
Wyss Institute at Harvard University
CLSB5, 3 Blackfan Circle
Boston, MA, 02115 USA
E-mail: don.ingber@wyss.harvard.edu

ABSTRACT

Many neurodevelopmental genetic disorders, such as Rett syndrome, are caused by a single gene mutation but trigger changes in expression and regulation of numerous other genes. This severely impair functions of multiple organs and organ systems beyond the central nervous system (CNS), adding to the challenge of developing broadly effective treatments based on a single drug target. This challenge is further complicated by the lack of sufficiently broad and biologically relevant drug screens, and the inherent complexity in identifying clinically relevant targets responsible for diverse phenotypes. Here, we combined human gene regulatory network-based computational drug prediction with *in vivo* screening in a population-level diversity, CRISPR-edited, *Xenopus laevis* tadpole model of Rett syndrome to carry out target-agnostic drug discovery, which rapidly led to the identification of the FDA-approved drug vorinostat as a potential repurposing candidate. Vorinostat broadly improved both CNS and non-CNS (e.g., gastrointestinal, respiratory, inflammatory) abnormalities in a pre-clinical mouse model of Rett syndrome. This is the first Rett syndrome treatment to demonstrate pre-clinical efficacy across multiple organ systems when dosed after the onset of symptoms, and network analysis revealed a putative therapeutic mechanism for its cross-organ normalizing effects based on its impact on acetylation metabolism and post-translational modifications of microtubules. Although traditionally considered an inhibitor of histone deacetylases (HDAC), vorinostat unexpectedly restored protein acetylation across both hypo- and hyperacetylated tissues, suggesting non-HDAC-mediated therapeutic mechanisms supported by proteomic analysis.

INTRODUCTION

Rett Syndrome (Rett) is a neurodevelopmental disorder that is also known to clinically impact multiple organs and systems in the body. It is primarily caused by mutations of the gene encoding methyl-CpG binding protein (MeCP2), a ubiquitous nuclear protein that acts as a transcriptional repressor and activator affecting hundreds of genes across the genome (Chahrour and Zoghbi, 2007). Rett is characterized by a high degree of cellular heterogeneity, with a mixture of wild type and MeCP2 mutant cells within the tissues of the same individual (Renthal et al., 2018) that leads to subtle but widespread gene misregulation (Gabel et al., 2015). Clinical criteria and research on Rett have primarily focused on neuromotor, social, and cognitive impairments and other CNS symptoms (e.g., seizures, repetitive purposeless movements, regression, microcephaly, loss of speech, autistic features)(Colvin et al., 2003; Kerr et al., 2001). However, these patients also commonly exhibit multiple clinical symptoms outside of the CNS, including respiratory dysfunction, gastrointestinal issues, systemic inflammation, disrupted metabolism, circadian rhythm and sleep disturbances, abnormal bone density, kidney function, nociception derangement, which are a major source of morbidity that contribute to a shortened lifespan (Hagberg, 2002; Vashi and Justice, 2019). It is important to note that although Rett is considered a neurodevelopmental disorder and therapeutics development has focused on CNS-related endpoints, these system-wide symptoms are often the most disturbing to patients and families, and thus there is a need to ameliorate symptoms of this disease across the entire body.

Monogenic diseases are theoretically amenable to gene therapy treatment, and Rett has been shown to be reversible in a mouse model of X chromosome reactivation (Przanowski et al., 2018) and post-natal expression of MeCP2 (Giacometti et al., 2007; Guy et al., 2007). However, even if current challenges around delivery efficacy and safety could be overcome, Rett and other X-linked disorders require gene dosage compensation to avoid toxicity due to

overexpression of the corrected gene since even a modest 20% deviation of MeCP2 expression levels can lead to Rett symptoms (Collins et al., 2004; Luikenhuis et al., 2004). Therefore, pharmaceutical treatments for Rett and other neurodevelopmental disorders are still needed. Trofinetide, a synthetic IGF-1 C-terminal tripeptide activating BDNF expression, has shown initial promise in phase II clinical trials and it progressed to phase III trials but demonstrated only moderate efficacy (Glaze et al., 2017). Sarizotan, a 5-HT1A and D2 receptor agonist with promising efficacy in mouse models of Rett (Abdala et al., 2014), was recently terminated after clinical trial results failed to demonstrate efficacy (NCT02790034). Esketamine, an N-methyl D-aspartate receptor (NMDAR) agonist, is also being evaluated in the clinic (NCT03633058) due to its reduction of neuroexcitatory glutamate. But these and other therapeutic paths for Rett pursued thus far target only a subset of patients' CNS symptoms and have not shown any effects on extra-CNS morbidity.

Here we present an integrated approach combining a novel gene expression network computational model to predict existing drugs and screening in an in vivo phenotypically diverse model of Rett syndrome generated in *Xenopus* tadpoles to assess whole-body efficacy. Our results led to the identification of vorinostat, which showed significant efficacy in a mouse Rett syndrome model even when initiating treatment after the onset of symptoms, demonstrating the utility of the target-agnostic platform for predicting drugs to restore multi-organ system function in Rett syndrome and potentially other complex diseases.

METHODS

X. laevis care and rapid generation of Rett syndrome tadpole models

Xenopus embryos and tadpoles were housed at 18°C with a 12/12 h light/dark cycle in 0.1X Marc's Modified Ringer's (MMR) medium. Tadpoles were fed 3x/week with sera Micron

97 Nature fry food. All animal experiments and procedures were reviewed and approved by the
98 Harvard Medical School (HMS) Institutional Animal Care and Use Committee regulations.
99 Xenbase (Nenni et al., 2019) (www.xenbase.org) was used to search for MeCP2 homolog in
100 *Xenopus laevis* (*Xenopus laevis* J-strain 9.2 version). MeCP2.L (XB-GENE-17346751),
101 MeCP2.S (XB-GENE-494744), found on Chromosome 8L and 8S, show 75% and 70%
102 sequence identity with human MeCP2, respectively. An important biological distinction is that
103 while human MeCP2 is found on the X chromosome, Chromosome 8 is not part of the sex
104 determination alleles of homomorphic chromosome pairs in *X. laevis*. Cas9 target sites were
105 selected using CHOPCHOP (Labun et al., 2016) on the *X. laevis* J-strain 9.2 version, which
106 facilitated the selection of guide RNA with no predicted off-targets. We used the default settings
107 to generate a list of target sequences. We selected 4 targets from this list for each of the L and
108 S forms. This selection was based primarily on the ranking provided by CHOPCHOP and as a
109 function of their location on MeCP2 to target exons coding for the methyl-CpG-binding domain
110 (MBD, exons 2 and 3) and Transcriptional repression domain (TRD, exon 3). The 8 sgRNA
111 sequences are presented in **Supplementary Table 9** and were synthesized as modified sgRNA
112 by Synthego Inc.

113 The sgRNA were resuspended to 100 µM in 0.1X Tris EDTA (pH 8.0). Then, an
114 equimolar sgRNA mix was made using 2 µl of each sgRNA, for a total of 16 ul. The Cas9 RNP
115 complex was formed by mixing 75 pmol of the sgRNA mix with 75 pmol of Cas9 in annealing
116 buffer (5 mM HEPES, 50 mM KCl, pH 7.5), for a total volume of 100 µL, then incubated at 37°C
117 for 10 minutes. The RNP was kept frozen at -20°C until the day of the injection. To generate
118 MeCP2 knockdown models of Rett syndrome, *Xenopus* embryos were fertilized and maintained
119 at 14°C until the 4-cell stage. Each cell was injected with ~2 nL RNP per injection resulting in a
120 final amount of 1.5 fmol of RNP per injection per cell, and we did not see any adverse effect
121 when controlling for Cas9 or sgRNA at that amount. Note that the 1.5 fmol of ribonucleoprotein

122 (RNP) used per injection is two to five time less than what has been commonly used in
123 previously published studies for *Xenopus* (Aslan et al., 2017) as we found that higher amounts
124 of sgRNA had adverse effects (not shown). Following injections, embryos were kept in 0.1X
125 MMR at 18°C as described above, for the 18 days duration of the experiment.

126 **PCR and fragment analysis to validate MeCP2 gene disruption**

127 MeCP2 editing efficiency was measured using Indel Detection by Amplicon Analysis
128 (Yang et al., 2015), which leverages PCR using a pair of primers and universal fluorescein
129 labeled oligo (**Supplementary Table 10**).The primers were synthesized by IDT. The amplicons
130 were purified (Zymo Research) and submitted for fragment analysis on an ABI 3730XL
131 (performed by Genewiz) following the IDAA method described previously. ProfileIT IDAA
132 analysis software (COBO Technologies) was used to analyze the fragments and visualize the
133 distribution of indels and visualize out-of-frame indels (Lonowski et al., 2017). IDAA is a robust
134 method with 1-bp resolution suited for the analysis of a tetraploid genome without the need for a
135 deep sequencing approach.

136 We analyzed the indels of 3 target sites on MeCP2.S of 14 tadpoles presenting with
137 seizures and 3 non-edited tadpoles. Using a window of +/- 100 bp from the target site, we
138 observed varied editing efficiencies depending on the target site. The likely out-of-frame indels
139 ratio averaged 47% for Xl-mecp2s-g01 on exon 3, with the lowest being 12% for a given tadpole
140 and highest being 95%, 48% for Xl-mecp2s-g02 on exon 2 (min/max 20-84%), and ~82% for Xl-
141 mecp2s-g04 on exon 2 (min/max 7-91%). Overall, 98% of indels where between 1 to 30 bp, and
142 84% were deletions.

143 **Microarray analysis**

144 Tadpoles were sacrificed at stage 50 of development and lysed using a QIAGEN
145 TissueLyser II bead mill (30 Hz, 2 x 30 sec) in a 2 mL tube with a 2.4 mm steel beads (Omni)

146 and 1 mL phosphate buffered saline buffer at 4ºC. 250 mL of lysate was used for RNA
147 extraction using a QIAGEN RNeasy mini kit. RNA samples were DNAse treated. *Xenopus laevis*
148 Genome 2.0 Array (Affymetrix) microarrays were processed by Advanced Biomedical
149 Laboratories (Cinnaminson, NJ). RNA samples were processed using a Nugen Ovation PICO
150 WTA System V2 kit. The resulting cDNAs were purified using a Qiagen MinElute PCR
151 Purification Kit following the modifications outlined in the Nugen protocol. The cDNAs were
152 fragmented and labeled using a Nugen Encore Biotin Module. Hybridization solutions were
153 prepared by combining the fragmented, biotin-labeled cDNAs with hybridization cocktail
154 (Affymetrix Hybridization, Wash, and Stain Kit). The mixtures were incubated in a thermal cycler
155 at 99 °C for 2 min followed by 45 °C for 5 min. then loaded on *Xenopus laevis* Genome 2.0
156 arrays and incubated for 16-20 hours at 45 ºC and 60 rpm in an Affymetrix Hybridization Oven
157 645. Following hybridization, arrays were washed and stained on Affymetrix Fluidics Station
158 450s using the Affymetrix FS450_0001 protocol with the stains and buffers supplied in the
159 Affymetrix Hybridization, Wash, and Stain Kit. The stained arrays were scanned at 532 nm
160 using an Affymetrix GeneChip Scanner 3000.

161 **Transcriptomics Data Processing**

162 Microarray datasets were RMA normalized. RNAseq gene counts were normalized using
163 size factors similar to the normalization performed by the R package DESeq. Genes missing
164 values were removed and duplicates were combined by taking the maximum across counts.
165 Gene expression heatmaps and hierarchical clustering plots were generated for all groups using
166 the R package limma (version 3.42.2) and Python package seaborn (version 0.9.0). Volcano
167 plots were generated using the Python package bioinfokit (version 0.7).

168 **nemoCAD Drug Prediction Algorithm**

169 In the present study, we developed the nemoCAD computational tool to predict drugs
170 that would shift MeCP2-edited tadpoles to a control tadpole state based on transcriptome state
171 for each condition. nemoCAD utilizes pre-computed interaction probabilities of drug-gene and
172 gene-gene interactions and differential gene expression signatures of a disease state and
173 appropriate control to identify compounds capable of changing a transcriptional signature
174 indicative of one biological state to another state of interest (e.g., reverting a disease state to a
175 healthy state).

176 The repurposing algorithm is first used to identify transcriptome-wide differential
177 expression profiles between two biological states in the input transcriptomic dataset
178 (experimental or published) and to define the target normalization signature, i.e., the subset of
179 genes whose expression levels need to be reversed in order to revert one state to the other
180 (e.g., normalize the diseased state). Pairwise analysis, that implicitly assumes genes are
181 expressed independently of one another, is carried out based on the comparison between gene
182 expression profiles of >19,800 compounds found in the LINCS database release v1
183 (Subramanian et al., 2017) and the target normalization signature. Multiple correlation statistics
184 (e.g., Pearson correlation, cross-entropy) across all differentially expressed genes are
185 calculated and a combination score (e.g., Pearson correlation divided by the cross-entropy) is
186 computed.

187 Putative predictions that incorporate gene-gene dependencies are then generated
188 separately based on Bayesian network analysis on a regulatory and drug-gene interaction
189 network architecture defined using publicly available databases of gene-gene interactions based
190 on single gene knockout datasets in human cells (KEGG, TRRUST) and reference
191 transcriptional signatures of drugs (LINCS, CTD), as described below. By combining a directed
192 unweighted network structure with interaction probabilities for the connecting network edges,
193 the constructed network is a weighted directed graph consisting of all possible paths that

connect at least 2 genes of interest from the relevant genes within the target transcriptomic normalization set and the drugs; it therefore encodes the entire region of influence of a given list of genes and the drugs that can reverse their gene expression profiles in the desired manner. This network is then used as input for a message-passing algorithm (e.g. loopy belief propagation algorithm (Forbes, 2021; Pearl, 1982)) in which the marginal probability distributions of drugs being “on” given the expression state of every gene are computed using the joint probability distribution encoded in the . This network-based approach leads to a ranking of all the drugs based on the probability of them inducing the desired transcriptomic signature across all genes in the network, which is separate from the initial ranking based on correlation analysis described above. This method has the advantage of incorporating gene-gene dependencies, but its success relies on the quality of network structures curated in the source databases.

Ultimately, drugs are prioritized that have both high correlation with the desired transcriptional signature change, representing desired drug-gene interactions, and high probabilities of being able to reverse the diseased state predicted by the Bayesian network analysis, representing gene network-level drug effects that can counter network-level disease processes. nemoCAD also enables visualization of the architecture of the network and subnetworks, and thus provides insight into potential molecular targets that can be verified using additional experiments. nemoCAD also can be used to optimize treatment regiments by iteratively inputting animal omics data following drug treatment to further tune drug predictions and develop drug combinations that might synergize in unpredictable ways. The approach underlying nemoCAD avoids the needs for *a priori* target or pathway inputs and, in fact, enables their discovery.

219 **Transcriptomics Gene Network Construction**

220 Gene regulatory networks were inferred from gene expression data using the
221 Bioconductor package GEne Network Inference with Ensemble of trees (GENIE3) release 3.12
222 in RStudio (R version 3.6.2)(Huynh-Thu et al., 2010). GENIE3 infers a weighted, directed gene
223 regulatory network from expression data by decomposing the prediction of a network between *k*
224 genes into *k* different regression problems. For each individual regression analysis, the
225 expression pattern of one of the genes (target gene) is predicted from the expression patterns of
226 all the other genes (regulator genes) using ensembles of regression trees. GENIE3 produces an
227 adjacency matrix representation of the network with *k* nodes in which each node represents a
228 gene, and an edge directed from one gene *i* to another gene *j* indicates that gene *i* regulates the
229 expression of gene *j*. Based on known mechanisms involved in Rett Syndrome
230 (**Supplementary Table 1**), a subset of genes was selected as candidate regulators: BDNF,
231 FCRL2, FMR1, MeCP2, NTRK2, PER1, PER2, and PUM1. These potential regulators were
232 calculated over all available target genes in the transcriptomics datasets (10,934 genes) for
233 MeCP2 knock down and cas9-injected control samples. Digraph objects were constructed from
234 adjacency matrices and visualized in Matlab R2020a (Mathworks; Natick, MA) for each of the
235 MeCP2 knock down and control groups. The strongest regulator gene-target gene relationships
236 were highlighted by filtering each network at a consistent edge weight (e_w) threshold ($e_w = 0.3$)
237 prior to plotting.

238 **Cross-Species Transcriptomics Analysis**

239 Gene networks involved in Rett Syndrome in human patients and MeCP2 knock down in
240 laboratory animal models were compared using previously acquired transcriptomics datasets
241 (**Supplementary Table 2**). Transcriptomics datasets were processed using the same methods
242 described for *Xenopus* transcriptomics and normalized using a series of transformations. Since
243 RNA-seq data typically have a wider dynamic range than microarray datasets, RNA-seq and

microarray data was transformed into a common space (Sekhon et al., 2013). RNA-seq datasets were transformed using a hyperbolic sine function and the $\log_2$ transformation was applied to microarray data (Sekhon et al., 2013). Subsequently, a variance stabilizing transformation was applied to remove potential mean-variance relationships in each dataset (Russo et al., 2018). Common genes expressed and measured between datasets (926 genes) were considered for further analysis. Dimensional reduction was performed using Principle Component Analysis (PCA) and visualized using Uniform Manifold Approximation and Projection (UMAP) in Python with the help of sklearn and UMAP packages.

Commonalities in gene expression values across species were analyzed by plotting heatmaps of differential gene expression using the Python packages seaborn and matplotlib. All datasets were normalized as described above and log fold change for each gene was calculated by combining samples of a condition using geometric mean. Log fold changes for all species were combined and the genes (96 genes) with variance greater than the mean variance (in fold changes) were used to construct the heatmaps.

Transcriptomics gene networks were constructed using GENIE3 and the same methods previously described. To investigate potential changes across the entire gene network, regulator genes were *not* down selected. Adjacency matrices were visualized for each network and the distribution of edge weights in the network was assessed by histogram and boxplots in Matlab. Digraph objects were constructed from adjacency matrices and visualized in Matlab for the strongest connections in each network (e_w > 99.99% for each network). Resultant networks were combined across all datasets for each species and plotted with different colors designating each dataset. A cross-species network that includes the strongest network connections across all datasets was formed by combining each species-specific dataset and plotted with different colors designating each species. To identify the strongest regulator and target gene nodes in the resultant cross-species network, the in-degree and out-degree were calculated in Matlab.

269 The in-degree is defined as the number of edges with that node as the target and out-degree of
270 a node is equal to the number of edges with that node as the source.

271 **Drug screening**

272 Drugs for tadpole screening were purchased from Sigma-Aldrich (St. Louis , MO, USA)
273 or MedChem Express (Monmouth Junction, NJ, USA) and dissolved in DMSO to a stock
274 concentration of 100-1,000 μM, depending on the solubility. For screens, compounds were
275 diluted to their final concentrations with a 0.1% DMSO concentration. Media with dosed drug
276 were made fresh and exchanged every two days following feeding. Dosing began at stage 45
277 and lasted for 7 days, after which standard 0.1X MMR was used to evaluate drug washout
278 effects. Free-swimming tadpoles were imaged in 60 mm dishes using a SONY Alpha a6100
279 camera with 16mm objective against an illuminated background. Tadpole behavior was scored
280 manually by noting the most severe seizure-related phenotype described by Hewapathirane et
281 al. (Hewapathirane et al., 2008) within a 20 min period.

282 Vorinostat and trofinetide for mouse studies were purchased from MedChem Express
283 (Monmouth Junction, NJ, USA). For intraperitoneal injection, trofinetide was solubilized in
284 DMSO, and vorinostat was solubilized in a method previously published(Basu et al., 2019;
285 Hockly et al., 2003). 2-hydroxypropyl-β-cyclodextrin powder (HPβCD) was purchased from
286 Acros Organics (ThermoFisher, Waltham, MA, USA). Vorinostat was dissolved in 100 mM
287 HPβCD by boiling for 5 minutes. Mice were dosed intraperitoneally at 100mg/kg with Trofinetide
288 and 50 mg/kg with vorinostat. For oral dosing, commercial instructions were followed to add
289 solubilized vorinostat (100 mg/kg) to Medigel (purchased from ClearH20, Westbrook, ME, USA).

290 ***X. laevis* Tissue Processing**

291 After stage 46 tadpoles were euthanized with 20x Tricaine, tadpoles were washed three
292 times with PBS (-/-) and fixed in 4% Paraformaldehyde in PBS + Mg + EGTA (MEMFA) (Alfa

293 Aesar, Tewksbury, MA, USA) for 2 hours at RT. For sections, *Xenopus* tadpoles were
294 cryoprotected by sequential incubation of 10%, 20% and 30% sucrose in 1x PBS(-/-), only
295 transferring to the subsequent concentration when the samples sunk to the bottom of the
296 scintillation vial. Cryoprotected tadpoles were embedded in 5% agarose and were stored in -
297 80°C. For GI staining, the gastrointestinal tract was microdissected with a stereoscope before
298 embedding. Embedding tissue were sectioned coronally at 20 µm thickness on a Cryostat
299 (Leica, CM3050 S, Wetzlar, Germany) and mounted on superfrost plus slides (Thermo Fisher,
300 Waltham, MA, USA). Slides were dehydrated for 30 minutes at 20°C, before storing at -80°C.
301 For whole mount preparation, tadpoles were processed in a method previously published
302 (Willsey, 2021).

303 ***In situ* hybridization**

304 Following X. *laevis* tissue processing of cryosections, sample pretreatment, RNAscope
305 Target Retrieval and the RNAscope Assay was conducted by the HMS Neurobiology Imaging
306 Facility following manufacturer's instructions. Xl.MeCP2 was custom designed by Advanced Cell
307 Diagnostics. Rpl8 was used as a positive control (Xl-LOC108706872-C3, Cat No. 516501-C3,
308 Advanced Cell Diagnostics, Hayward, CA) and DapB as a negative control (Cat No. 320758,
309 Advanced Cell Diagnostics, Hayward, CA).

310 **Immunohistochemistry of *Xenopus laevis* sections and whole mounts**

311 Following tissue processing, cryosections were blocked for 2 hours at room temperature
312 and subsequently incubated with primary antibodies overnight at 4°C, including mouse anti-
313 alpha acetylated tubulin (1:1000 dilution, Sigma Aldrich, Burlington, MA USA), mouse anti-beta-
314 tubulin (1:1000 dilution, E7, Developmental Studies Hybridoma Bank, Iowa City, Iowa, USA),
315 anti-MeCP2 (1:1000 dilution, Invitrogen, Waltham, MA USA), Hoechst (1:1000 dilution,

316 ThermoFisher, Waltham, MA, USA), negative controls anti-mouse IgG (1:1000 dilution,
317 Invitrogen, Waltham, MA, USA), and anti-rabbit (1:1000 dilution, Invitrogen, Waltham, MA USA),
318 as well as FITC-conjugated isolectin B_4 (1:1000 dilution, Thermo Fisher, Waltham, MA, USA).
319 Slides were washed twice with TRIS-buffered saline, with 1% Tween-20 (TBT) for 5 minutes
320 each and incubated in the dark with their corresponding secondary antibody: Goat anti-rabbit
321 Alexa 647 (1:1000 dilution, Abcam, Waltham, MA, USA) and Goat anti-mouse Alexa 594
322 (1:1000 dilution, Abcam, Waltham, MA, USA) for 1 hour at room temperature. Slides were
323 washed three times with TBT for 5 minutes each on an orbital shaker and mounted in ProLong
324 Gold Antifade Mountant (ThermoFisher, Waltham, MA, USA) with a #1 coverslip and sealed.
325 Slides were stored in the dark at 4°C before image acquisition. Z-stacks were acquired at 1μm
326 to visualize brain and gastrointestinal sections.

327 *X. laevis* embryos were processed for whole mount immunofluorescence as described
328 (Willsey, 2021). Fixed tadpoles were quenched for 1 hour in a lightbox in 5% formamide and 4%
329 hydrogen peroxide in PBS, permeabilized for 1 hour in PBS with 0.1% Triton X-100 (PBT) and
330 blocked for 1 hour in 10% CAS-Block in PBT (Life Technologies, Carlsbad, CA, USA). Primary
331 antibodies were incubated overnight at 4°C, including mouse anti-alpha acetylated tubulin
332 (1:700 dilution Sigma Aldrich, Burlington, MA USA), mouse anti-beta-tubulin (1:100 dilution, E7,
333 Developmental Studies Hybridoma Bank, Iowa City, Iowa, USA)), Hoechst (1:100 dilution,
334 ThermoFisher, Waltham, MA, USA) and anti-mouse IgG (1:100 dilution). Slides were washed in
335 PBT, blocked in 10% CAS-Block for 30 minutes, and incubated with the corresponding
336 secondary antibody for 2 hours at room temperature including Goat anti-mouse Alexa 546
337 (1:100 dilution, Thermo Fisher, Waltham, MA, USA) and Goat anti-rabbit 633 (1:100 dilution,
338 ThermoFisher, Waltham, MA, USA). Tadpoles are washed with PBT for 1 hour and then
339 washed in PBS for another hour before mounting in Vectashield (Vector Laboratories,

340 Burlingame, CA, USA). Z-stacks were acquired at 1μm for visualizing epidermal MCC's and
341 3μm for visualizing entire brain regions.

342 **Drug target discovery in *X. laevis* using thermal proteome profiling**

343 *Sample preparation*

344 While we largely followed the protein integral solubility alteration (PISA) thermal
345 proteome profiling protocol (Gaetani et al., 2019), we adapted the mammalian cell- and tissue-
346 specific parameters to tadpoles by optimizing the method to tadpoles by reducing thermal
347 treatment temperatures to account for the lower normal temperature range of *X. laevis*.
348 Unmodified *X. laevis* tadpoles (stage 47-50) were exposed to 25 μM vorinostat or 0.1 μM
349 ivermectin for 2 h while freely swimming in 0.1x MMR medium. Following euthanasia using
350 Tricaine, animals were washed with fresh MMR, cut into thirds (head, abdomen containing all
351 visceral organs, and tail), and placed into individual Eppendorf tubes covered with MMR
352 containing the same drug and concentration and incubated for 3 min at one of 9 temperatures
353 spanning 30-60°C. 30°C was selected as the control temperature, where no appreciable thermal
354 denaturation should take place, based on the maximum tolerable temperature for *X. laevis*
355 (Ruthsatz et al., 2018). Following aspiration of remaining liquid, samples were flash frozen in
356 liquid nitrogen.

357 Samples were further processed and analyzed by Phenoswitch Bioscence, Inc.
358 (Sherbrooke, Québec, Canada). Thermally-treated samples were lysed in 100 µL PBS with
359 0.4% NP-40 with 4 cycles of freeze/thaw. Insoluble material was cleared by centrifugation (10
360 min, 10,000 G, 4°C). 11µL of supernatant for each of the 9 temperatures were then pooled in
361 one tube and samples were centrifuged again at 13,000 RPM for 75 minutes, at 4°C to pellet
362 precipitated proteins. 80 µL of the supernatant were reduced with 10 mM DTT for 15 min at
363 65°C and alkylated with 15 mM IAA and 30 min at room temperature in the dark. Proteins were

364 precipitated with 8 volumes of ice-cold acetone and 1 volume of ice cold methanol overnight.
365 Protein pellets were washed 3 times with 250 µl of ice-cold methanol and resuspended in 100
366 µL digestion buffer. Digestion was carried for 4 hours in 50 mM Tris ph 8 + 0.75 mM Urea + 1µg
367 trypsin/LysC at 37°C with agitation. Another 1 µg of trypsin/LysC was added, and digestion was
368 continued overnight. Peptides were purified by reversed phase SPE and analyzed by LC-
369 MS/MS.

370 *Mass spectrometry*

371 Acquisition was performed with a TripleTOF 6600 (Sciex, Foster City, CA, USA)
372 equipped with an electrospray interface with a 25 µm iD capillary and coupled to a Micro LC200
373 (Eksigent, Redwood City, CA, USA). Analyst TF 1.8 software was used to control the
374 instrument. Acquisition was performed in data independent acquisition (DIA or SWATH) using
375 gas phase fractionation (GPF1 from 350 m/z to 800 m/z and GPF2 from 800 m/z to 1250 m/z).
376 The source voltage was set to 5.5 kV and maintained at 325oC, curtain gas was set at 45 psi,
377 gas one at 25 psi and gas two at 25 psi. Separation was performed on a reversed phase
378 Kinetex XB column 0.3 µm i.d., 2.6 µm particles, 150mm long (Phenomenex) which was
379 maintained at 60°C. Samples were injected by loop overfilling into a 5 µL loop. For the 60
380 minutes LC gradient, the mobile phase consisted of the following solvent A (0.2% v/v formic acid
381 and 3% DMSO v/v in water) and solvent B (0.2% v/v formic acid and 3% DMSO in EtOH) at a
382 flow rate of 3 µL/min. Both GPF files were analyzed on a previously-generated 3D ion library
383 using the SWATH 2.0 microapp from Peakview (Sciex, Foster City, CA, USA). Each GPF file
384 was analyzed using 10 peptides per protein, 4 MS/MS transition per peptide, 12.5 min RT
385 window and 25 ppm XIC width. The reported quantification for a protein is the sum of all the
386 correctly integrated peptides (FDR<0.05) in both GPF files.

387 **Mouse care**

388 Experiments were performed with MeCP2-null (*MeCP2*$^{-/Y}$) (strain 003890) and age-
389 matched WT male littermates (*MeCP2*$^{+/Y}$), purchased from Jackson Laboratories (Bar Harbor,
390 ME). All mice were housed in ventilated racks under specific-pathogen-free conditions at a room
391 temperature in a 12/12 h light/dark cycle with food and water ad libitum. All animal experiments
392 and procedures were reviewed and approved by the Harvard Medical School (HMS) Institutional
393 Animal Care and Use Committee regulations. Every effort was made to minimize their suffering.
394 Mice were assessed for disease severity and endpoint criteria on a daily basis by weighing and
395 using the phenotypic scoring method developed by the Bird laboratory (Guy et al., 2007;
396 Szczesna et al., 2014), which includes assessing mobility, gait, breathing, tremor, and general
397 condition. Endpoint was determined by 20% body mass loss or a score of 2 in criteria D, E, or
398 F. Dosing and Behavioral procedures began when mice reached 4 weeks of age.

399 **Behavioral Testing**

400 *Elevated Plus Maze (EPM)*

401 The elevated plus maze (EPM) consisted of two open and two closed (34 cm long and 5
402 cm wide) arms extended out from a central platform 50 cm above the floor. The test was carried
403 out in dim ambient lighting. The room of the experiment and its spatial cues were kept
404 consistent and minimal. Mice were habituated in the test room for 30 minutes before the start of
405 the test. Mice were placed near the center compartment of the maze, facing an open arm, and
406 allowed to explore the apparatus for 5 minutes. After each test, the maze was cleaned
407 thoroughly with 70% ethanol and left to dry before the start of the next test. A computer-assisted
408 video-tracking system (EthoVision XT 14, Noldus, Leesburg, VA) was used to record the
409 number of open and closed arm entries as well as the total time spent in open, closed, and
410 center compartments. An increase in the percent time spent or entries into the open arms was
411 used as a surrogate measure of anxiolytic-like behavior (Carobrez and Bertoglio, 2005).

412 *Spatial Novelty Y-Maze (Y-maze)*

413 The spatial novelty y-maze consisted of a Y-shaped maze with three arms at a 120° from
414 each other as well as a removable blockade used to prevent access to one of the arms during the
415 Habitutation phase. The test was carried out in dim ambient lighting. The room of the experiment
416 and its spatial cues were kept consistent. One of the three arms was defined as the start arm,
417 where the mice would be placed at the start of the experiment and was kept consistent throughout
418 the entire study. The test consisted of a three-minute Habituation phase where one of the two
419 non-start arms was blocked off, a two-minute intertrial interval (ITI) outside of the maze and a
420 three-minute Test phase, where the previously blocked arm was exposed to the mouse. The arm
421 that was blocked off during the Habituation phase was randomized and noted for each mouse.

422 Mice were kept in an adjacent room to not disturb the test. The test mouse was placed in
423 a holding cage and brought to the test room with the maze and immediately placed into the Y-
424 maze at the designated start arm and allowed to explore the start and familiar arm trial for three
425 minutes. At the end of the habituation phase, the mouse was placed into the holding cage for 2
426 minutes ITI. During this time, the blockade was removed, and the maze was cleaned with an
427 ammonia-based cleaner with a paper towel and left to dry to remove odor cues. The mice were
428 then placed back in the start arm and left to explore the entire maze for three minutes. After the
429 test trial, the mouse was transported back to its home cages and the maze was again wiped dry
430 with an ammonia based cleaner. A computer-assisted video tracking system (EthoVision XT 14,
431 Noldus, Leesburg, VA) was used to record the number of entries, time spent in each arm and as
432 distance traveled in each arm during the Habituation and Test Phase. The percentage of time and
433 distance spent in the novel, or previously blocked arm were used to assess spatial novelty seeking
434 behavior (Dellu et al., 2000).

435

436 **Mouse Histology and Immunostaining**

437 Mice were euthanized with CO_2 inhalation, transcardially perfused with PBS (-/-) and 4%
438 PFA, and tissues of interest were removed. Regions of the gastrointestinal tract and lung
439 processed as was described previously(Morton and Snider, 2017; Nalle et al., 2019; Tsai et al.,
440 2017). Paraffin blocks were sectioned into 15 μm thickness. Mouse lung tissues were sectioned
441 coronally and GI tissues were stained with hematoxylin and eosin (H&E) by the Beth Israel
442 Deaconess Medical Center's IHC Core Facility. The slides were also stained for rabbit anti-
443 acetylated α-tubulin (ABclonal, ab179484, Woburn, MA, USA) mouse anti-CD-64 (R&D systems,
444 AF3628, Minneapolis, MN, USA), chicken anti-βIII-tubulin (Biolegend, 801202, San Diego, CA,
445 USA) immunofluorescence by Beth Israel Deaconess Medical Center's IHC Core Facility.

446 Mouse brains were fixed with 4% paraformaldehyde at 4°C overnight, cryoprotected in a
447 sucrose gradient (10%, 20% and 30%), and subsequently embedded in OCT Tissue Tek. The
448 embedded tissues were subsequently sectioned coronally at 30μm and the free-floating sections
449 were stained as previously described(Potts et al., 2020). The sections were blocked with 10%
450 CAS Block in PBT for 1hr, stained with primary antibody (rabbit anti-iba-1, 1:1000, Wako, #019-
451 19741; mouse anti-NeuN, 1:1000, Abcam, #ab104224; Hoechst, 1:1000, Thermo Fisher, H1399)
452 overnight at 4°C. After three 10-minute washes in PBS (-/-) on an orbital shaker, the sections were
453 stained in secondary antibody (anti-rabbit Alexa 647 for iba1, anti-mouse Alexa 594 for NeuN) for
454 1 hour at room temperature. After three 10-minute washes on an orbital shaker, the sections were
455 mounted on superfrost plus slides (ThermoFisher, Waltham, MA, USA) in ProLong Gold Antifade
456 Mountant (ThermoFisher, Waltham, MA, USA) with a #1 coverslip and sealed. Z-stack images
457 were acquired at 1μm intervals using the 63x/ glycerol.

458

459

460 **Multiplex Chemokine Assay**

461 After mouse euthanization, blood was collected by cardiac puncture using at 23G needle
462 in ethylendiamine tetra-acetic acid (EDTA) treated tubes (Microvette 200 K3EDTA, CAT#
463 20.1288.100, Sarstedt, Numbrecht, Germany). To avoid hemolysis, the tubes were kept at room
464 temperature and quickly processed for plasma. Tubes were centrifuged at 2000 x g for 10
465 minutes and the plasma was separated and stored in -80C until assayed. Chemokine levels
466 were measured in mouse plasma using the Bio-Plex Pro Mouse Chemokine Panel 31-Plex
467 (Cat# 12009159, Bio Rad, Hercules, CA, USA). Measurements were performed using the Bio-
468 Plex 3D Suspension Array System (BioRad, Hercules, CA, USA), following the manufacturer's
469 instructions.

470 **Microscopy and Image Processing**

471 H&E slides were imaged with 4x and 20x objectives with the Biotek Cytation 5.
472 Immunofluorescent *Xenopus* whole mounts and *Xenopus* and mouse stained sections were
473 imaged with the Leica SP5 X MP Inverted Confocal Microscope using 25x (NA 0.95) water
474 objective and 63x (NA 1.3) Glycerol objectives. Sections were imaged in white light and diode
475 laser scanning mode and whole mounts were imaged using multiphoton pulsed IR laser
476 scanning. Serial scanning was used during acquisition to avoid bleed-through. Image settings
477 were kept constant between groups, in terms of laser power, bit-depth, z-stack interval,
478 resolution (pixels), aperture settings, and gain/offset. Images were post-processed and
479 analyzed using ImageJ (Fiji, NIH).

480 *MCC morphological analysis*

481 2-photon images of X. laevis 25x and 63x MCC's were maximum projected, background
482 subtracted, and subsequently assessed for cilia orientation and cilia length, as previously
483 described (Chien et al., 2018).

484 *MCC Functional Assay*

485 We visualized the cilia-driven flow of fluorescent microspheres over the surface of the xenopus
486 tadpole by taking times series with the Leica SP5 x MP inverted confocal. Our methods were
487 based on previous reports (Kulkarni et al., 2018) with some modifications. Stage 45 tadpoles
488 were placed in a 24 well μ-Plate 14mm (ibidi, Gräfelfing, Germany), and underwent anesthesia
489 by incubation with 1x tricaine before proceeding to image. One tadpole was placed per well for
490 individual tracking. Fluorescent microspheres beads (Thermo Fisher, Waltham, MA) were added
491 at a final dilution of 1:100. We chose the bead size of 3μm, because during preliminary testing
492 and as is reflected in the data, WT *X. laevis* tadpoles consistently was able to clear beads that
493 were 3μm diameter at this concentration. The Leica SP5 x MP laser scanning mode was used
494 to visualize the fluorescent microspheres beads at an excitation of 520nm and emission of
495 560nm with the following settings: 512x512 pixels, bidirectional scanning mode, and at a scan
496 speed of 800-1600Hz, with the 25x (NA 0.95) water objective, and over the time course of 5
497 minutes every 5s. Time series were acquired of in the olfactory and lateral region of the
498 epidermis.

499 *Quantification of bead displacement*

500 The time series stacks were maximum intensity projected to visualize the overall bead flow.
501 Intensity was measured as a function from the distance from the surface of the epidermis.

502 *Mean Intensity Quantitation*

503 To generate a ROI mask, channels acquired in one z-stack were split and the maximum
504 intensity projection of a 'control' channel was taken. In the case for assessing αaT expression
505 mouse GI tract and bronchiole, the βIII-tubulin channel was used, and for assessing MeCP2
506 expression, the α -acetylated tubulin channel was used in the image stack. Subsequently,
507 background noise was subtracted, and auto-thresholded, whose settings were held constant

508 between groups. The ROIs generated from the control channel were used to quantify the
509 maximum projected channel of interest, to obtain the mean intensity (integrated density per
510 area). A minimum of 3 serial sections were analyzed per animal.

511 *Counting Ib4+ cells*

512 Confocal Z-stacks of *X. laevis* GI tract images were quantified for IB4+ cells, by taking the
513 maximum intensity projection of the ib4+ channel. Following noise reduction, and auto-
514 threshold, ib4+ cells were segmented and counted using the particle analysis function in the
515 ImageJ software (NIH, Bethesda, MD).

516 *Sholl Analysis*

517 Sholl analysis was performed as previously published[47]. Confocal (at 1um intervals) Z-stacks
518 were maximum intensity projected in the iba-1 channel, noise de-speckled, subsequently
519 segmented using the auto-threshold function, and microglia were duplicated into 8-bit TIF files,
520 in the field of view, ensuring that for each mouse at least 10 microglia were selected in the
521 ipsilateral and contralateral region of the olfactory bulb. Using the Sholl analysis plugin in
522 ImageJ (NIH, Bethesda, MD), traces and intersections were generated.

523 **Statistical analysis**

524 Statistical analysis of biological results was performed using Graphpad Prism 9.3. For
525 comparison of two conditions, Student's t-test was used unless otherwise indicated. ANOVA
526 with pairwise t-tests and Bonferroni correction or the Holm-Šídák tests was used to evaluate
527 significance of multiple variables. P values <0.05 were considered significant (*, $p < 0.05$; ** $p <$
528 0.01; *** $p < 0.001$; **** $p < 0.0001$). Tadpole screens and mouse studies were conducted with
529 5-8 animals each and repeated, except for the mouse oral dosing study.

530

531 **RESULTS**

532 **Modeling Rett syndrome genetic and phenotypic heterogeneity in *Xenopus laevis***

533 A major challenge to Rett therapeutics discovery lies in the inherent heterogeneity
534 observed in patients stemming from gene expression variability due to the gene regulatory
535 impact of distinct MeCP2 mutations, combined with tissue heterogeneity caused by mosaicism
536 resulting from X chromosome inactivation. As a result, Rett patients exhibit a spectrum of
537 disabilities. To establish an animal model of Rett that would incorporate the heterogeneity
538 observed in patients, we used CRISPR to generate a mosaic knockdown of MeCP2 protein in
539 *Xenopus laevis* tadpoles, which have been previously used to model neurodevelopmental
540 diseases due to their evolutionary proximity to mammals and well-characterized neural
541 development (Exner and Willsey, 2021; Pratt and Khakhalin, 2013).

542 Injection of *X. laevis* embryos at 4- or 8-cell stages using cas9 pre-complexed with
543 sgRNA targeting 6 sites of the MeCP2 gene, including the regions corresponding to the DNA-
544 binding domain, resulted in a tunable model of MeCP2 knockdown with a heterogeneous
545 phenotype when assessed at the population level. Based on our target selection and injection
546 strategy at the 4-cell stage, each individual animal was edited as a mosaic and presented
547 varying degree of severity, without apparent toxicity from Cas9 or sgRNA. Indeed, all embryos
548 developed to the swimming tadpole stages (Nieuwkoop-Faber stages 45-50) with no apparent
549 loss of viability or morphological defect in earlier stages.

550 Importantly, swimming tadpoles with MeCP2 knock down ("Rett" tadpoles) exhibited a
551 broad range of abnormal behavior compared to wild type vehicle-injected control tadpoles
552 ("Control") including darting motions and rapid repetitive swimming in tight circles (**Fig. 1a,b and**
553 **Supplementary Movie 1**) reminiscent of the repetitive motions observed in human Rett patients
554 as well as C-shaped or straight rigor (**Supplementary Movie 1**) that has been shown to

555 correspond to seizures in prior *Xenopus* studies (Hewapathirane et al., 2008). The cas9 protein
556 and sgRNA doses were titered to achieve between 5 and 95% gene editing efficiency as
557 determined by qPCR without resulting in toxicity (**Supplementary Fig. 1a**). All tadpoles
558 exhibited significant MeCP2 gene insertion/deletion polymorphisms (indels) at each of the
559 mecp2 gene target sites (**Supplementary Fig. 1b**) and reduced MeCP2 RNA expression (**Fig.**
560 **1c**). MeCP2 protein levels were also heterogeneously reduced in the brain (**Fig. 1d,e**) and
561 olfactory multiciliated cells (MCC) (**Fig. 1d,f**). This this editing approach resulted in an animal
562 model of Rett with intra-subject and inter-subject diversity at molecular and phenotypic scales,
563 which is similar to what is observed in humans.

564 In line with prior studies in humans and other model organisms (Sanfeliu et al., 2019, p.
565 2), when we analyzed the transcriptome-wide effects of MeCP2 knockdown on the Rett
566 phenotype in *Xenopus*, only subtle shifts in gene expression were detected with 70 out of
567 10,935 genes probed undergoing a significant change in gene expression ($p_{adjusted}<0.05$) (**Fig.**
568 **1g, Supplementary Table 1**). Of the 70 differentially expressed genes, 37 are involved in
569 metabolic processes, 9 operate within developmental processes, and 8 are part of signal
570 transduction pathways (**Supplementary Fig. 2a**); this aligns with changes in genes that control
571 metabolism or regulate neuronal processes (e.g., ion transport, nervous system development) in
572 Rett patients (Renthal et al., 2018).

573 Interestingly, analysis of gene co-expression networks identified substantial
574 reorganization from control animals (**Fig. 1h**) following MeCP2 knock down (**Fig. 1i**),
575 characterized by a loss of strong connectivity among genes involved in the regulation of MeCP2
576 (FMR1 and TRKB receptor NTRK2 (Abuhatzira et al., 2007; Arsenault et al., 2021)), neuronal
577 development (BDNF (Chang et al., 2006; Li and Pozzo-Miller, 2014)),, and circadian rhythm
578 (PER1, PER2 (Martínez de Paz et al., 2015)) all of which are altered in Rett patients (Li and
579 Pozzo-Miller, 2014; Miller et al., 2019). Notably, after MeCP2 knock down, BDNF strengthened

580 as a network hub and exhibited greater co-expression connectivity amongst gene nodes (**Fig.**
581 **1i**).This was unexpected because although BDNF is involved in neuronal development, synaptic
582 transmission, and plasticity, it declines with the onset of Rett-like neuropathological and
583 behavioral phenotypes (Li and Pozzo-Miller, 2014). However, BDNF is a known target of
584 repression by MeCP2 and our findings are consistent with prior work suggesting that
585 downregulation of BDNF is a later and indirect outcome of MeCP2 deficiency (Chang et al.,
586 2006; Li and Pozzo-Miller, 2014).

587 We then comprehensively compared the effects of MeCP2 knock down in *Xenopus* to
588 changes observed in published transcriptomic data sets from Rett patients as well as MeCP2
589 knockout mouse and zebrafish models (**Supplementary Table 2**). After performing
590 dimensionality reduction in this cross-species analysis, *K*-Means clustering applied to the
591 principal components revealed 3 clusters, with mouse and human clustering together and
592 zebrafish and *Xenopus* forming 2 independent clusters (**Supplementary Fig. 2b**). Importantly,
593 diverse gene-expression abnormalities that occur across cell types in Rett syndrome could
594 contribute to the differences observed across these datasets (Renthal et al., 2018). In this case,
595 both the human and mouse transcriptomics were performed on brain tissues, whereas the
596 zebrafish and *Xenopus* data are from whole organisms, which may account for the clustering
597 patterns observed.

598 Despite evidence of species-specific clustering, a common gene signature comprised of
599 96 genes was identified across all species by searching for genes with a fold change variance
600 greater than mean variance. However, the common genes within this transcriptomic signature
601 are expressed at similar low fold change levels in 7 of the 9 datasets analyzed, with slightly
602 greater variations in expression only observed in 1 out of 5 mouse datasets and 1 out of 3
603 human datasets (**Fig. 1j**). This finding provides additional evidence that mutation of MeCP2
604 produces widespread, yet subtle, perturbations in gene expression.

605 Using gene co-expression network analysis (Huynh-Thu et al., 2010), we also identified
606 interconnected gene sub-networks that are conserved across species and tissues in the MeCP2
607 deficient condition (**Fig. 1k, Supplementary Tables 3 and 4**). Comparison across all species
608 identified several shared major gene targets and regulators despite differences in species-
609 specific network structure (**Supplementary Fig. 2c**). Interestingly, WNT8B, which is known to
610 be modulated by the Rett-implicated gene Foxg1 (Aguiar et al., 2014), was found to be the most
611 interconnected gene target within the MeCP2 cross-species network. The strongest gene
612 regulators in this network, NR4A3 and SOD2, are both involved in oxidative metabolism, which
613 is also known to be dysregulated in Rett Syndrome (De Felice et al., 2012)**.** Thus, this CRISPR-
614 enabled *Xenopus* model of Rett replicates many genetic and phenotypic features of the disease
615 seen in humans.

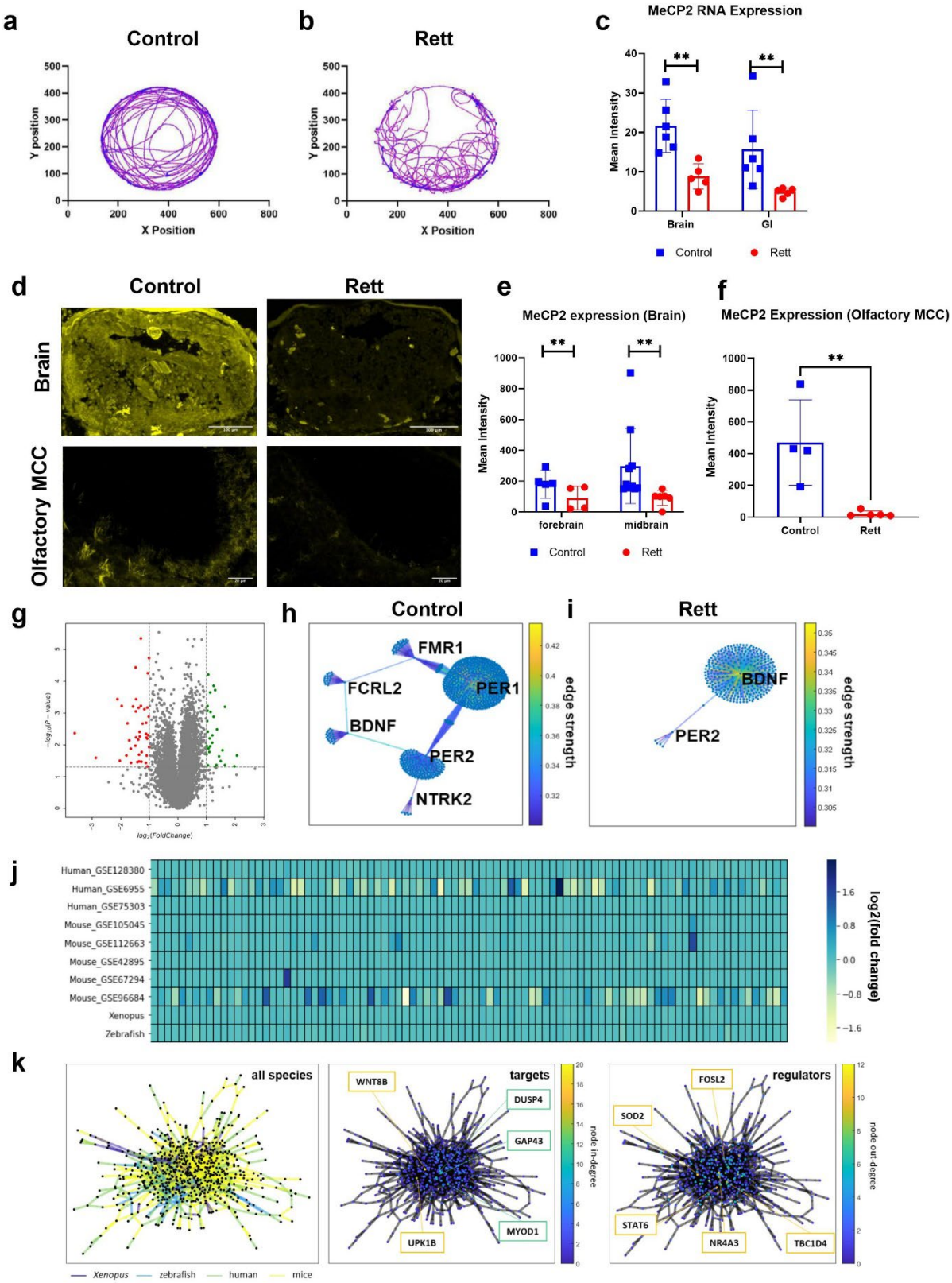
a
Control
Y position
X Position
b
Rett
Y position
X Position
c
MeCP2 RNA Expression
Mean Intensity
Brain
GI
Control
Rett
d
Control
Rett
Brain
Olfactory MCC
e
MeCP2 expression (Brain)
Mean Intensity
forebrain
midbrain
Control
Rett
f
MeCP2 Expression (Olfactory MCC)
Mean Intensity
Control
Rett
g
h
Control
FMR1
FCRL2
PER1
BDNF
PER2
NTRK2
edge strength
i
Rett
BDNF
PER2
edge strength
j
Human_GSE128380
Human_GSE6955
Human_GSE75303
Mouse_GSE105045
Mouse_GSE112663
Mouse_GSE42895
Mouse_GSE67294
Mouse_GSE96684
Xenopus
Zebrafish
log2(fold change)
k
all species
Xenopus
zebrafish
human
mice
targets
WNT8B
DUSP4
GAP43
UPK1B
MYOD1
node in-degree
regulators
FOSL2
SOD2
STAT6
NR4A3
TBC1D4
node out-degree

616

617 **Figure 1: MeCP2 knockdown using CRISPR in *Xenopus laevis* tadpoles models Rett**
618 **syndrome. a-b,** Tadpole models of Rett syndrome exhibit distinct swimming behavior in 60 mm
619 diameter dishes following MeCP2 knockdown ("Rett") compared to mock-injected controls
620 ("Control"). MeCP2 RNA expression in brain and gastrointestinal (GI) tract using RNAscope, **c**,
621 and protein in brain and multi-ciliated olfactory cells using immunohistochemistry, **d-f**, are
622 significantly reduced in Rett syndrome tadpole models while maintaining a large degree of
623 heterogeneity spatially, **d**, and across tissues, **e-f**; scale bars, 100 μm in brain, 20 μm in
624 olfactory multi-ciliated cells. **g**, Volcano plot of differentially expressed genes showing that only
625 70 genes are significantly up- or down-regulated following MeCP2 knockdown ($p < 0.05$, fold
626 change >2, t-test with Bonferroni correction, N = 3). Gene regulatory networks for control, **h,** and
627 Rett, **i,** tadpoles reveal large network rearrangements with an increase in BDNF centrality. **j**,
628 Comparison against other Rett syndrome models and clinical samples indicates minimal
629 differential gene expression across the 96-gene signature developed to classify Rett syndrome.
630 **k**, Network-level comparison across species and tissues (left) and identified shared target
631 (middle) and regulator (right) genes.

632

633 **Computational discovery of drugs that reverse the network-level impact of Rett**

634 In Rett, MeCP2 knockout results in widespread but subtle gene expression patterns, and
635 most effects are not detectable using standard statistical analysis. Researchers have applied
636 network-based analytical methods to uncover previously-hidden connections within RNA and
637 protein interaction networks (Miller et al., 2019; Sanfeliu et al., 2019; Varderidou-Minasian et al.,
638 2020), but these approaches have not been applied to Rett syndrome therapeutics discovery.
639 To leverage transcriptomics analysis for drug discovery, we developed a computational
640 framework we termed nemoCAD (network model for causality-aware discovery)(**Fig. 2a**) that
641 compares transcriptomic signatures of disease versus healthy control subjects to predict

642 compounds from the Library of Integrated Network-Based Cellular Signatures (LINCS) database
643 ("NIH LINCS Program," n.d.), including FDA-approved drugs, which have a high likelihood to
644 reverse the disease signature state back to a healthy state. Though signature-based tools have
645 been previously developed to enable drug discovery (e.g., CMAP (Lamb et al., 2006), NicheNet
646 (Browaeys et al., 2020), GPSnet (Cheng et al., 2019)), a major drawback is the impact of the
647 expression of any single gene or protein on the resulting prediction. To be used effectively,
648 these tools require well-matched disease datasets to the human cell line-based datasets
649 present in LINCS, which may not be feasible for many diseases.

650 In contrast, we pursued an entirely different approach to transcriptomics signature
651 analysis that is based on a Bayesian network encoding directed gene-gene and drug-gene
652 interactions. By leveraging data in LINCS containing transcriptomics results following single
653 gene knockout/knockdown and overexpression as well as addition of drug perturbagens in
654 human cells, we calculated the probabilities of pairwise interactions among all of the genes and
655 drugs in a human gene-gene and drug-gene interaction network whose structure was extracted
656 from Comparative Toxicogenomics Database (CTD) ("The Comparative Toxicogenomics
657 Database | CTD," n.d.), KEGG (Kanehisa and Goto, 2000), and TRRUST (Han et al., 2018).
658 Unlike signature based computational tools that take gene expression signatures at face value,
659 this probabilistic approach offers greater abstraction while prioritizing for the network impact of
660 perturbations, including those caused by disease or addition of drugs, and thereby reduces the
661 impact of tissue-specific or species-specific transcriptomic biases as well as the influence of the
662 expression of any individual gene.

663 To identify drugs that might reverse disease states, we generated probabilistic network
664 maps for each drug in the aggregate 19,800+ compound dataset. By inputting and comparing
665 gene microarray data from MeCP2 knockdown tadpoles versus vehicle-injected controls, we
666 identified sets of differentially expressed genes contained within the gene-gene interaction

667 network with a p-value < 0.05 and a log2 fold change between 0.7 and 3.1 in 0.3-fold-change
668 increments. For each fold-change, we generated a ranked list of compounds predicted to induce
669 reversal of transcriptome-wide changes of: 1) single gene states using a cross-correlation score,
670 2) single gene states using a cross-entropy score, and 3) an overall gene network state score
671 corresponding to the probability of involvement of the drug nodes in the identified subnetwork.
672 These drug lists were combined to identify drugs that were ranked by being most consistently
673 predicted to reverse the Rett transcriptome-wide changes and robust across the computational
674 settings (**Supplementary Table 5**). Drugs were manually down-selected based on available
675 toxicity data and to prioritize chemical diversity for initial screening. Rett tadpoles or controls
676 were then dosed with lead compounds for 7 days via the culture medium beginning 1-2 days
677 after the onset of symptoms and after collecting baseline swimming behavior data. Animal
678 behaviors (swimming pattern abnormalities and seizure stages) were recorded every other day
679 during drug exposure and washout phases, and the severity of seizure-like events was used as
680 a screening metric.

681 These studies revealed that the FDA-approved drugs, vorinostat and ivermectin,
682 demonstrated time-dependent reductions in seizure score that reversed after the drugs were
683 washed out (**Fig. 2b**; **Supplementary Fig. 3**). However, we focused on vorinostat rather than
684 ivermectin in all subsequent studies due to its higher predicted scoring consistency over time,
685 more favorable reported pharmacokinetics, and its ability, albeit limited, to cross the blood-brain
686 barrier. As a positive control with which to gauge relative efficacy, we also evaluated trofinetide,
687 the synthetic IGF-1 C-terminal tripeptide. Although only moderately effective in recent Phase III
688 Rett syndrome clinical trial top-line results that aligned with Phase II trial outcomes (Glaze et al.,
689 2017), trofinetide represents the most relevant clinical-stage benchmark treatment. Importantly,
690 in our Rett tadpole models, both trofinetide and vorinostat reduced seizure-like phenotypes and
691 also increased viability (**Fig. 2b**). At day 6 of treatment, there was a statistically significant effect
692 by both drugs on reducing swimming score relative to baseline before treatment onset (**Fig. 2c**).

693 As expected, no significant change was seen in WT and Rett vehicle-treated animals. This
694 head-to-head comparison has supported the possibility that our *Xenopus* population-level model
695 of Rett can offer predictive value for drug development.
696

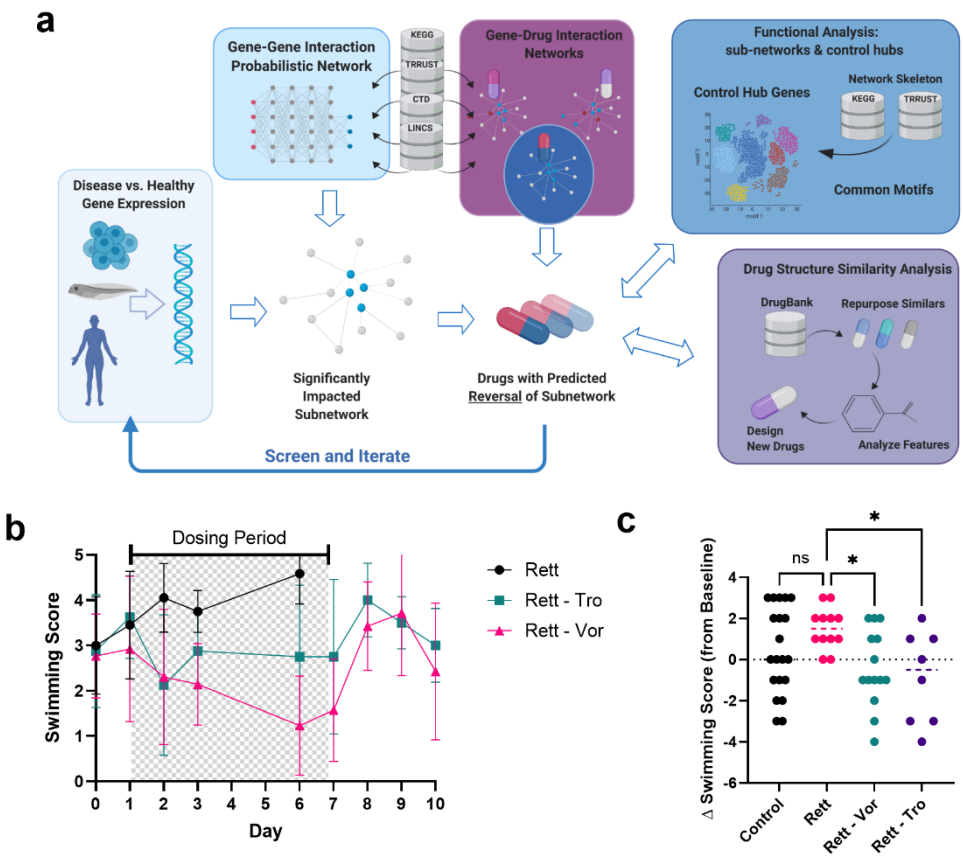

Figure 2: Network-based computational prediction of effective drugs to treat Rett syndrome in tadpole models. a, Network model for causality-aware discovery (nemoCAD) combines a directed gene-gene and drug-gene interaction network extracted from CTD, TRRUST, and KEGG databases with interaction probabilities inferred from single gene and drug perturbations in LINCS. Transcriptome data from any disease model or patient and corresponding control are used to identify the relevant subnetwork and disease-specific “node weights” that account for probabilities of up-/down-regulation of a gene. A drug-gene interaction probability matrix, inferred from LINCS, is computationally screened against the disease-specific subnetwork to identify compounds that significantly interact with the subnetwork and are ranked by their predicted ability to restore the disease transcriptome back to a healthy state based on single gene and gene network signatures. Downstream analyses can be performed on the

709 resulting gene-gene interaction subnetwork by interrogating the underlying subnetwork structure
710 to find control nodes and other network metrics. Additionally, the chemical structures of the
711 predicted drugs can be clustered by structural similarity based on SMILES notation and
712 annotated protein targets and pathways from DrugBank data. **b**, Graph showing relative effects
713 on seizure score over 10 days of treatment in MeCP2 KD tadpoles of vehicle and 25 μM
714 vorinostat (Rett - Vor) versus 70 μg/mL trofinetide (Rett - Tro), a clinical-stage drug with
715 demonstrated efficacy (tadpoles per condition and timepoint: N = 12 Rett - Vor and Vehicle, N =
716 8 Rett - Tro; error bars indicate s.d.; ANOVA P = 0.028 Vehicle-treated MeCP2 KD tadpoles did
717 not survive past day 3 of the treatment period in one study and past day 6 in a second study. **c**,
718 Change in swimming score at day 6 of treatment vs. baseline (day 0) is significantly improved
719 by both drugs. *, P < 0.05.

720

721

722 To understand the protein targets of both drugs, we adapted thermal proteome profiling
723 (Franken et al., 2015; Huber et al., 2015; Mateus et al., 2017) that identifies molecules that
724 drugs bind directly to protein targets for use with a whole exothermic animal (*Xenopus* tadpole)
725 as well as using isolated body segments (head, viscera, tail). While we were able to detect
726 some of the known histone deacetylase (HDAC) targets of vorinostat, we also found that both
727 this drug and ivermectin bind to multiple other proteins related more broadly to acetylation
728 metabolism, beyond histones and HDACs (**Supplementary Table 6**). These findings suggest a
729 potential mechanism of action for the Rett normalizing responses we observed that involves
730 restoration of normal acetyl-CoA metabolism and post-translational acetylation.
731 As these observations initially aligned with results of prior studies of HDAC6 acetylation
732 of tubulin in cells of Rett patients (Gold et al., 2015; Lebrun et al., 2021) and microtubule
733 modulation in closely-related CDKL5 deficiency disorder (Barbiero et al., 2019), we analyzed

734 tadpole tissues for α-tubulin acetylation and observed surprising bidirectional shifts in
735 acetylation patterns depending on the tissue type. For example, α-tubulin was hypoacetylated in
736 neurons in sections of the midbrain (**Supplementary Fig. 4a**) and hindbrain (**Fig. 3f**) and
737 increased in GI tract (**Fig. 3g**) and olfactory multi-ciliated cells (**Supplementary Fig. 4b**) and
738 following MeCP2 knockdown, resulting in more sparse but dense tangles. Higher resolution
739 imaging revealed that the cilia were longer and misaligned on multiciliated cells compared to
740 controls (**Fig. 3a**), and both length (**Fig. 3b**) and orientation (**Fig. 3c**) were restored by
741 vorinostat treatment.

742 We then evaluated the impact of ciliary morphology and organization on ciliary function
743 using fluorescent microparticles (**Supplemental Fig. 5**). The disruption of ciliary beating-
744 induced flow on the surface of skin (**Fig. 3d**) and olfactory multiciliated cells (**Fig. 3e**) due to
745 MeCP2 knockdown is reversed by vorinostat treatment, suggesting that ciliary function
746 restoration is linked to ciliary function.

747 Due to the prevalence of GI symptoms in Rett patients and our observation of tubulin
748 acetylation disruption and vorinostat-induced recovery in the GI tract (**Fig. 3g**), we further
749 explored the role of MeCP2 knockdown in the gut. Staining for isolectin B4-positive (ib4+) cells
750 to assess GI tract inflammation and nociceptive innervation, which is increased in Rett patients
751 (Baikie et al., 2014; Downs et al., 2010), revealed that tadpoles exhibited significant ib4+
752 expression due to MeCP2 knockdown (**Fig. 3h,i)**, which vorinostat again reversed.
753
754

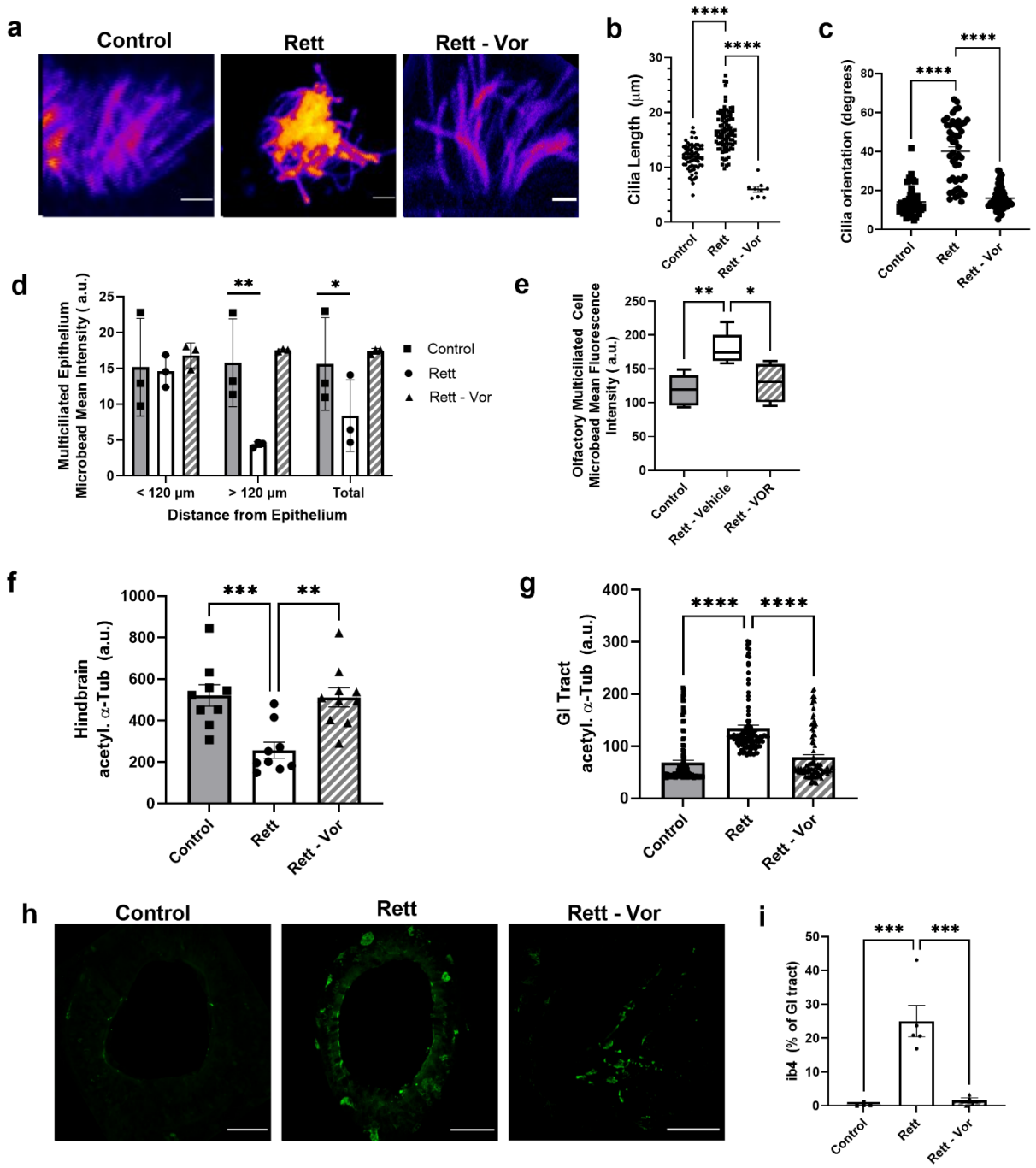

755

756

757

758

759

760

761 **Figure 3: Vorinostat treatment of Rett tadpoles restores ciliary function, normalizes hypo-**
762 **and hyperacetylated tubulin across tissues, and reduces GI tract inflammation. a,**
763 Olfactory cell ciliary abnormalities due to MeCP2 knockdown were restored by treatment with
764 vorinostat (magenta-yellow colormap of fluorescence intensity, cilia stained for tubulin),
765 significantly restoring their **b,** length and **c,** orientation (****, $P < 0.0001$). Functional rescue of
766 cilia was also observed in both epithelial, **d**, and olfactory multiciliated cells in a microbead
767 clearance assay (*, $P < 0.05$; **, $P < 0.01$). Despite the canonical HDACi activity of vorinostat,
768 both hypoacetylated tubulin in the hindbrain, **f**, as well as hyperacetylated tubulin in the GI tract,
769 **g**, was normalized. **h**, immunifluorescence images and **i**, plot showing that the % of ib4+ cells in
770 the GI tract of tadpoles is increased in Rett tadpoles, which is indicative of inflammation and
771 heightened pain response, and that this can be rescued by vorinostat treatment.

772

773 **Vorinostat normalizes the Rett phenotype in a mouse model**

774 Because vorinostat was predicted to reverse the Rett state in our computational studies,
775 we evaluated its efficacy in the MeCP2-deficient male (*MeCP2*$^{-/Y}$) mouse Rett model that is
776 commonly used in pre-clinical studies for Rett therapeutics, including trofinetide (Guy et al.,
777 2001). We first treated younger animals starting at day 31 post-partum (p31) as was done in
778 previous studies and confirmed that daily intraperitoneal (i.p.) administration of trofinetide (100
779 mg/kg) results in significant amelioration of multiple disease-related parameters, including
780 diarrhea and motor function, measured by a reduction in the established Bird score (Guy et al.,
781 2007) that incorporates a broad range of Rett-related CNS and non-CNS symptoms. When
782 vorinostat (50 mg/kg) and trofinetide were similarly administered i.p. on a daily basis over two
783 weeks and compared with vehicle control, we found that animals responded favorably to both
784 drugs (**Fig. 4a**); however, treatment with vorinostat resulted in improved neurological function
785 compared to trofinetide, as determined by measuring elevated plus maze (EPM) performance

786 (**Fig. 4b**). Both drugs also resulted in enhanced spatial novelty Y-maze performance (**Fig. 4c**)
787 and an improved diarrhea score (**Fig. 4d**).
788 As brain microglia have been implicated in Rett progression and therapeutic effects
789 (Cronk et al., 2015; Derecki et al., 2012; Schafer et al., 2016) based on their role in
790 neuroinflammation, waste removal, and synaptic pruning, we immuno-stained for microglia
791 using ionized calcium binding adaptor molecule (Iba-1), a microglia-specific marker, in sections
792 of MeCP2$^{-/y}$ mouse brains. Using Sholl analysis to assess microglia morphology (Timmerman et
793 al., 2018), we found that the MeCP2$^{-/y}$ microglia exhibited significantly stunted morphology with
794 fewer projection crossings compared to WT littermates, indicative of a heightened inflammatory
795 state, which vorinostat restored (**Fig. 4e,f**). This result, together with the reduction of multiple
796 serum inflammatory markers, including TNF-α, IL-4, IL-6, IL-16, CCL2, MIP3b, and CCl1 (**Fig.**
797 **4g**), suggests that animals with Rett experience a heightened inflammatory state, and that
798 treatment with vorinostat can suppress this inflammation.
799

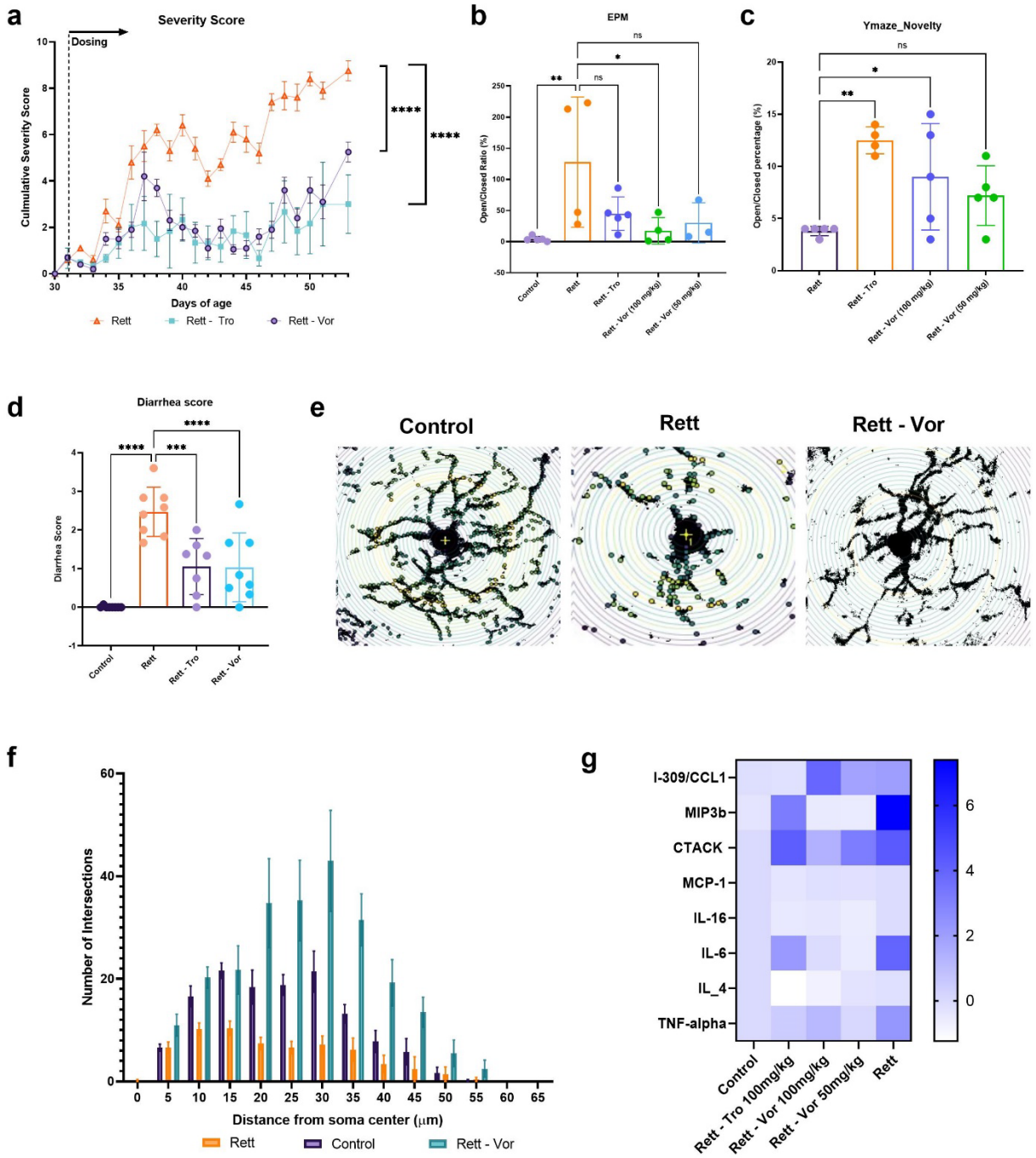

Figure 4: Vorinostat rescues multiple Rett syndrome-related CNS and somatic symptoms. a, Bird severity scores measured in MeCP2$^{-/Y}$ mice treated with vehicle (Rett),

805 trofinetide (100 mg/kg), or vorinostat (50 mg/kg) from day 31 to 51 of age (ANOVA; ****, P <
806 0.0001). **b,** elevated-plus maze and, **c**, Y-novelty maze cognitive tests of MeCP2$^{-/Y}$ mice
807 comparing vorinostat treatment efficacy to vehicle and trofinetide (ANOVA and Holm-Šídák test;
808 *, P < 0.05; **, P < 0.01). **d**, diarrhea scored using a 0-3 scale (ANOVA and Holm-Šídák test;
809 ***, P < 0.001; ****, P < 0.0001). Representative images of Sholl analysis of microglial
810 arborization in mouse olfactory (**e**) and the Sholl analysis graph showing the branching profile of
811 microglia (**f**) in control versus Rett mice treated with or without vorinostat (ANOVA and Holm-
812 Šídák test; Control vs. Rett, P = 0.0004; Control vs. Vor, P < 0.0001). **g**, Levels of indicated
813 cytokines measured in plasma of control mice versus Rett mice with or without treatment with
814 trofinetide (Rett – Tro, 100 mg/kg), vorinostat (Rett – Vor, 50 mg/kg), or vehicle (Rett) for 3
815 weeks (mean values shown, N = 3, scale at right indicates z-score normalized to wild-type
816 vehicle-treated littermates). The observed baseline inflammatory state in Rett mice agreed with
817 published effects of MeCP2 knockdown(O'Driscoll et al., 2015).
818

819 **Oral vorinostat exhibits broad efficacy in Rett mice even after onset of symptoms**

820 Pre-clinical studies for Rett therapies routinely dose MeCP2$^{-/y}$ mice prior to the onset of
821 symptoms (Castro et al., 2014; Szczesna et al., 2014) due to the rapid onset of symptoms and
822 short lifespan of animals, in contrast to patients who seek clinical care due to developmental
823 deficits which may not be diagnosed for several years before treatment could be initiated
824 (Tarquinio et al., 2015). To better mimic this more relevant clinical scenario, male MeCP2$^{-/y}$
825 mice were dosed approximately one week after the onset of symptoms. Also, because long term
826 treatment of Rett patients would be best served by oral administration, and due to the fact that
827 our results showed a reduction in diarrhea in mice treated with vorinostat via daily i.p., we tested
828 the efficacy of an oral formulation of vorinostat. Interestingly, when we administered trofinetide
829 i.p. after symptoms developed in this model, it was found to be ineffective based on overall Rett
830 score, similar to the moderate efficacy observed in human clinical trials, whereas oral vorinostat

831 (50 mg/kg) prevented significant worsening of the symptom severity score (**Fig. 5a**), ameliorated
832 weight gain, and increased performance in EPM (**Fig. 5b**) and Y mazes (**Fig. 5c**). Animals
833 treated with oral vorinostat showed complete survival after 3 weeks of treatment, which is
834 comparable to what would be expected for vehicle-treated Rett animals for a study of this
835 duration, whereas only ~ 60% of trofinetide-treated Rett animals survived (**Fig. 5d**). To our
836 knowledge, this represents the first effective treatment of MeCP2$^{-/y}$ mice when treatment is
837 initiated *after* the onset of symptoms.

838 Rett patients and mouse Rett models exhibit significant declines in fine motor and gait
839 control as well as GI tract dysfunction(Hagberg, 2002; Motil et al., 2012). Importantly, the
840 deficiencies in mobility, gait, and hindlimb clasping, as well as increased diarrhea we also
841 observed in MeCP2$^{-/y}$ animals were again rescued by vorinostat treatment (**Fig. 5e,f**). Breathing
842 also was significantly improved following vorinostat treatment compared to trofinetide and
843 vehicle treatments (**Fig. 5g**). Given the putative effects of vorinostat on acetylation metabolism
844 and post-translational modification of tubulin and its disruption of ciliary function identified in
845 tadpoles, we also analyzed α-tubulin acetylation in the multi-ciliated cells in mouse lung
846 bronchioles, which revealed an overall increase of hyperacetylated α-tubulin in MeCP2$^{-/y}$
847 animals that vorinostat again restored (**Fig. 5h**). In addition, we explored the potential link of
848 tubulin acetylation with muscle function and found that vorinostat treatment can rescue the
849 disrupted α-tubulin acetylation observed in femoral muscle sections (**Fig. 5i**). Increased
850 acetylation due to the loss of MeCP2 may play a role in muscle function as hyperacetylation has
851 been shown to increase stiffness and resistance in striatal muscles *in vitro* (Coleman et al.,
852 2021).

853 We continued to evaluate the possible impact of tubulin acetylation by examining the
854 colon, a biomechanically-active organ that is often distended in Rett patients and may play a
855 major role in digestive tract disruption that is a major complaint of these patients clinically (Motil

856 et al., 2012). Initial histological analysis of the colon indicated a greater degree of vacuolization
857 and heightened neutrophil infiltrate in MeCP2-null animals, which vorinostat and trofinetide
858 reversed (**Fig. 5j**). Staining of these sections for βIII- and acetylated α-tubulin also revealed that
859 acetylated α-tubulin is significantly more colocalized with neuronal staining in the colon in
860 MeCP2-null mice, and that this can be normalized by treatment with either vorinostat or
861 trofinetide (**Fig. 5j**). However, while vorinostat also normalized the ratio of acetylated α-tubulin
862 to βIII-tubulin, it was unexpectedly worsened by trofinetide (**Fig. 5j,k**). While the developing GI
863 tract of tadpoles prevented detailed analysis of their enteric neurons, the tubulin acetylation-
864 normalizing effect of vorinostat identified by network analysis in *Xenopus* clearly translated to
865 this mammalian (mouse) model at the cellular level.

866 These data show that oral dosing of vorinostat improved classical disease outcome
867 metrics in MeCP2-null male mice and it ameliorated microglial dysfunction and hyperacetylation
868 of tubulin in their GI and respiratory tracts as well as in skeletal muscle. Vorinostat also was
869 recently shown to be effective in treating Fragile X syndrome (Ding et al., 2021), which is closely
870 related to Rett, sharing both X-linked mutations and symptoms of autism, although it is caused
871 by a mutation in the FMR1 gene. Interestingly, we identified a loss of gene network connectivity
872 with FMR1 in the Rett-related *Xenopus* gene network (**Fig. 1h**), and genes with the maximum
873 variation and fold change differences in humans with Fragile X also occurred in pathway classes
874 involved in oxidative stress and multiple biosynthesis pathways that align with the major
875 regulators we identified by the cross-species MeCP2 mutant network analysis (**Supplementary**
876 **Figure 6a** and **Supplementary Tables 7 and 8**). Moreover, when we used nemoCAD to predict
877 drugs that might reverse the Fragile X genotype in humans, both the compound classes and
878 gene targets were similar to those predicted for *Xenopus* with MeCP2 knockdown, including a
879 high number of PPAR receptor agonists, HDAC inhibitors, and cyclooxygenase inhibitors
880 (**Supplementary Figure 6b,c**). Thus, these computational results suggest more broadly that

881 developmental therapeutics approaches for neurodevelopmental disorders with similar broad
882 transcriptional effects may benefit from using this form of gene interaction network analysis to
883 identify network-level signatures characteristic of specific diseases and to predict drugs that
884 may reverse those changes.
885

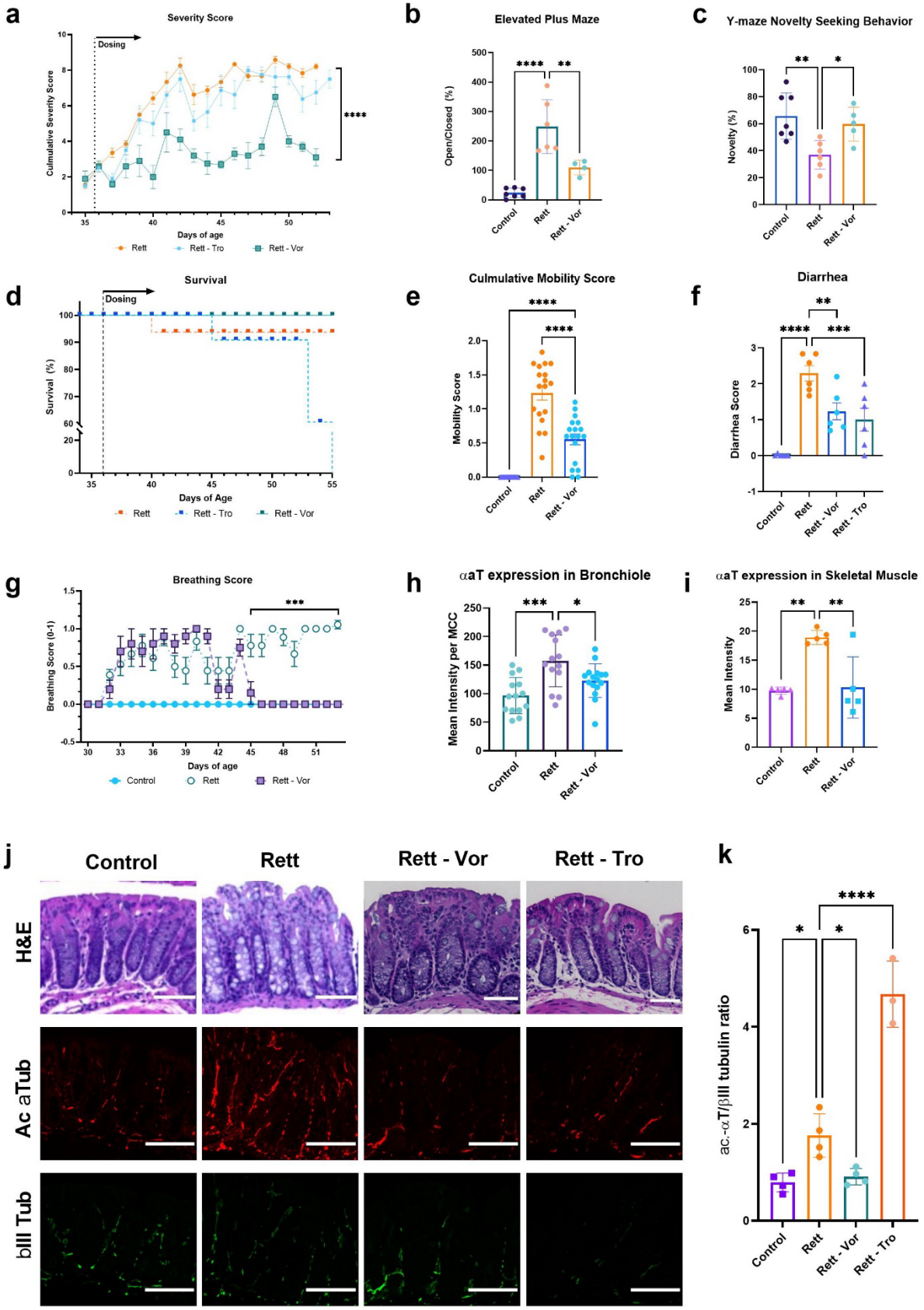
a
Severity Score
Dosing
Culmulative Severity Score
Days of age
****
Rett
Rett - Tro
Rett - Vor
b
Elevated Plus Maze
Open/Closed (%)
****
**
Control
Rett
Rett - Vor
c
Y-maze Novelty Seeking Behavior
Novelty (%)
**
*
Control
Rett
Rett - Vor
d
Survival
Dosing
Survival (%)
Days of Age
Rett
Rett - Tro
Rett - Vor
e
Culmulative Mobility Score
Mobility Score
****
****
Control
Rett
Rett - Vor
f
Diarrhea
Diarrhea Score
**
****
***
Control
Rett
Rett - Vor
Rett - Tro
g
Breathing Score
Breathing Score (0-1)
***
Days of age
Control
Rett
Rett - Vor
h
αaT expression in Bronchiole
Mean Intensity per MCC
***
*
Control
Rett
Rett - Vor
i
αaT expression in Skeletal Muscle
Mean Intensity
**
**
Control
Rett
Rett - Vor
j
Control
Rett
Rett - Vor
Rett - Tro
H&E
Ac aTub
bIII Tub
k
ac.-αT/βIII tubulin ratio
****
*
*
Control
Rett
Rett - Vor
Rett - Tro

886

887 **Figure 5: Oral administration of vorinostat in MeCP2$^{-/y}$ mice after the onset of Rett**
888 **symptoms rescues CNS and somatic symptoms. a,** Bird severity scores measured in
889 MeCP2$^{-/Y}$ mice treated with vehicle (Rett), trofinetide (100 mg/kg i.p.), or oral vorinostat (50
890 mg/kg) from day 36, after onset of symptoms, showing significant suppression of symptoms by
891 vorinostat treatment while trofinetide's effects were indistinguishable from the vehicle control
892 (ANOVA, ****, P < 0.0001). **b,** elevated-plus maze and, **c**, Y-novelty maze cognitive tests of
893 MeCP2$^{-/Y}$ mice comparing vorinostat treatment efficacy to vehicle and trofinetide (ANOVA and
894 Dunnett's multiple comparison test; *, P < 0.05; **, P < 0.01; ****, P < 0.0001). **d**, survival curve
895 of animals in this study. **e**, mobility scored using a 0-2 scale and **f**, diarrhea scored using a 0-3
896 scale (ANOVA and Holm-Šídák test; **, P < 0.01 ***, P < 0.001; ****, P < 0.0001). **g**, breathing
897 difficulty evaluated using a 0-1 score (ANOVA and Dunnett's multiple comparison test; ***, P <
898 0.001). Graphs showing levels of hyperacetylated α-tubulin in cells of the multi-ciliated cells in
899 the bronchiolar epithelium of the lung (**h**) and skeletal muscle (**i**) in mice treated as described in
900 **a** (data are presented as mean ± s.d.; *, P < 0.05; **, P < 0.01; ***, P < 0.001). **j**, Hematoxylin
901 and eosin (H&E) stained histological sections of colon from the control and drug-treated mice
902 (top row) and immunofluorescent staining for acetylated α-tubulin (middle) and βIII-tubulin
903 (bottom) in these sections. **k**, Graph showing changes in the βIII-tubulin ratio in drug-treated
904 versus control colon tissues (*, P < 0.05; ****, P < 0.0001).
905

906 **DISCUSSION**

907 Taken together, our results demonstrate the value of combining computational network
908 analysis-based drug repurposing algorithms with CRISPR technology to rapidly build novel *in*
909 *vivo* disease models using *X. laevis* that can be used to generate data and carry out screening
910 of drugs with activities of interest predicted computationally. The *Xenopus* tadpole model
911 developed here, which was generated in our laboratory within 3 weeks, exhibits a large degree

912 of genetic and phenotypic heterogeneity that reduces risks associated with computational and
913 screening outcomes by better capturing the disease state. Importantly, the *Xenopus* results
914 translated well to a mouse Rett model, and hence the tadpole model offers a faster, lower-cost,
915 and potentially much higher throughput alternative to mammalian models. In addition, our
916 target-agnostic computational approach enabled rapid discovery of novel mechanisms,
917 including the counterintuitive ability of an HDAC inhibitor to normalize both hypoacetylated
918 tubulin in the CNS and hyperacetylated tubulin in other organs, as well as identify drugs that
919 have broad efficacy across multiple organs. This approach led to the first demonstration of
920 efficacy in the mouse MeCP2 knockout model of Rett syndrome even when treated after the
921 onset of symptoms, in contrast with the lack of efficacy of trofinetide. Given the modest efficacy
922 of trofinetide in the clinic, conducting pre-clinical studies to restore health after the onset of
923 symptoms as in our *Xenopus* screen may be a more robust benchmark for efficacy in complex
924 CNS disorders. The drug discovery platform presented here offers Rett and other
925 neurodevelopmental patients the possibility of single small molecule therapeutics that address
926 multiple fundamental disease-modifying pathways with a broad clinical impact. Furthermore, by
927 identifying and rapidly evaluating existing drugs, potentially even in patients, our platform
928 enables the discovery of hidden therapeutic mechanisms for new drug development.
929

930 **ACKNOWLEDGEMENTS**

931 We would like to thank Dr. Barbara J. Caldarone for guidance and assistance with the
932 mouse neurobehavioral assays, Dr. Amanda Graveline, Sarai Bardales, Andyna Vernet and
933 Melissa Sanchez-Ventura for their assistance with mouse studies, Thomas C. Ferrante for
934 guidance and assistance with image acquisition and analysis, Dr. Lay-Hong Ang and Suzanne
935 White for tissue immunostaining support, Dr. Aurelien Begue and Mahmoud El-Rifai for their
936 assistance with RNAscope experiments, and Erin Switzer and Emma Lederer for help with

Xenopus embryo fertilization and husbandry. All behavioral experiments were conducted at the HMS Mouse Behavioral Core facility. M.L. gratefully acknowledges support of the Elisabeth Giauque Trust, London. We are grateful for funding from the Wyss Institute for Biologically Inspired Engineering at Harvard University through Validation Project support.

COMPETING INTERESTS

RN, FV, EG, ML, and DEI hold equity in Unravel Biosciences, Inc.; RN, FV, and DEI are members of its board of directors; ML and DEI are members of its scientific advisory board; and RN, FV, and EG are current employees of the company.

AUTHOR CONTRIBUTIONS

RN, FV, and DEI conceived of and directed the work. RN, TL, MS, FV, EG, KS, KV, and AV conducted animal studies and in vitro analyses. FV, MS, and VK developed and performed CRISPR generation of Rett tadpole models with guidance by ML. SK, MS, SL, VC, and TT performed bioinformatic analysis and computational drug prediction. SL and RN designed and developed nemoCAD software. JRT guided GI tract and lung immunostaining studies and evaluated the histology and tissue staining. RN and DEI wrote the manuscript. All authors reviewed and provided input for the manuscript.

DATA AVAILABILITY

All data used in this study, including the *Xenopus* microarray data, are publicly available using accession codes listed in **Supplementary Table 2**.

CODE AVAILABILITY

Code is available upon reasonable request to the corresponding author.

958 **REFERENCES**

959 Abdala AP, Lioy DT, Garg SK, Knopp SJ, Paton JFR, Bissonnette JM. 2014. Effect of Sarizotan, a 5-HT1a
960 and D2-Like Receptor Agonist, on Respiration in Three Mouse Models of Rett Syndrome. *Am J*
961 *Respir Cell Mol Biol* **50**:1031–1039. doi:10.1165/rcmb.2013-0372OC
962 Abuhatzira L, Makedonski K, Kaufman Y, Razin A, Shemer R. 2007. MeCP2 Deficiency in the Brain
963 Decreases BDNF Levels by REST/CoREST-Mediated Repression and Increases TRKB Production.
964 *Epigenetics* **2**:214–222. doi:10.4161/epi.2.4.5212
965 Aguiar DP, Sghari S, Creuzet S. 2014. The facial neural crest controls fore- and midbrain patterning by
966 regulating Foxg1 expression through Smad1 activity. *Development* **141**:2494–2505.
967 doi:10.1242/dev.101790
968 Arsenault J, Hooper AWM, Gholizadeh S, Kong T, Pacey LK, Koxhioni E, Niibori Y, Eubanks JH, Wang L-Y,
969 Hampson DR. 2021. Interregulation between fragile X mental retardation protein and methyl
970 CpG binding protein 2 in the mouse posterior cerebral cortex. *Hum Mol Genet* **29**:3744–3756.
971 doi:10.1093/hmg/ddaa226
972 Aslan Y, Tadjuidje E, Zorn AM, Cha S-W. 2017. High-efficiency non-mosaic CRISPR-mediated knock-in and
973 indel mutation in F0 Xenopus. *Development* **144**:2852–2858. doi:10.1242/dev.152967
974 Baikie G, Ravikumara M, Downs J, Naseem N, Wong K, Percy A, Lane J, Weiss B, Ellaway C, Bathgate K,
975 Leonard H. 2014. Gastrointestinal dysmotility in Rett syndrome. *J Pediatr Gastroenterol Nutr*
976 **58**:237–244. doi:10.1097/MPG.0000000000000200
977 Barbiero I, De Rosa R, Kilstrup-Nielsen C. 2019. Microtubules: A Key to Understand and Correct Neuronal
978 Defects in CDKL5 Deficiency Disorder? *Int J Mol Sci* **20**:4075. doi:10.3390/ijms20174075
979 Basu T, O'Riordan KJ, Schoenike BA, Khan NN, Wallace EP, Rodriguez G, Maganti RK, Roopra A. 2019.
980 Histone deacetylase inhibitors restore normal hippocampal synaptic plasticity and seizure

981 threshold in a mouse model of Tuberous Sclerosis Complex. *Sci Rep* **9**:5266.
982 doi:10.1038/s41598-019-41744-7
983 Browaeys R, Saelens W, Saeys Y. 2020. NicheNet: modeling intercellular communication by linking
984 ligands to target genes. *Nat Methods* **17**:159–162. doi:10.1038/s41592-019-0667-5
985 Carobrez AP, Bertoglio LJ. 2005. Ethological and temporal analyses of anxiety-like behavior: The elevated
986 plus-maze model 20 years on. *Neurosci Biobehav Rev*, Defensive Behavior **29**:1193–1205.
987 doi:10.1016/j.neubiorev.2005.04.017
988 Castro J, Garcia RI, Kwok S, Banerjee A, Petravicz J, Woodson J, Mellios N, Tropea D, Sur M. 2014.
989 Functional recovery with recombinant human IGF1 treatment in a mouse model of Rett
990 Syndrome. *Proc Natl Acad Sci U S A* **111**:9941–9946. doi:10.1073/pnas.1311685111
991 Chahrour M, Zoghbi HY. 2007. The Story of Rett Syndrome: From Clinic to Neurobiology. *Neuron* **56**:422–
992 437. doi:10.1016/j.neuron.2007.10.001
993 Chang Q, Khare G, Dani V, Nelson S, Jaenisch R. 2006. The disease progression of Mecp2 mutant mice is
994 affected by the level of BDNF expression. *Neuron* **49**:341–348.
995 doi:10.1016/j.neuron.2005.12.027
996 Cheng F, Lu W, Liu C, Fang J, Hou Y, Handy DE, Wang R, Zhao Y, Yang Y, Huang J, Hill DE, Vidal M, Eng C,
997 Loscalzo J. 2019. A genome-wide positioning systems network algorithm for in silico drug
998 repurposing. *Nat Commun* **10**:1–14. doi:10.1038/s41467-019-10744-6
999 Chien Y-H, Srinivasan S, Keller R, Kintner C. 2018. Mechanical Strain Determines Cilia Length, Motility,
1000 and Planar Position in the Left-Right Organizer. *Dev Cell* **45**:316-330.e4.
1001 doi:10.1016/j.devcel.2018.04.007
1002 Coleman AK, Joca HC, Shi G, Lederer WJ, Ward CW. 2021. Tubulin acetylation increases cytoskeletal
1003 stiffness to regulate mechanotransduction in striated muscle. *J Gen Physiol* **153**:e202012743.
1004 doi:10.1085/jgp.202012743

1005 Collins AL, Levenson JM, Vilaythong AP, Richman R, Armstrong DL, Noebels JL, David Sweatt J, Zoghbi HY.
1006 2004. Mild overexpression of MeCP2 causes a progressive neurological disorder in mice. *Hum*
1007 *Mol Genet* **13**:2679–2689. doi:10.1093/hmg/ddh282
1008 Colvin L, Fyfe S, Leonard S, Schiavello T, Ellaway C, Klerk N de, Christodoulou J, Msall M, Leonard H.
1009 2003. Describing the phenotype in Rett syndrome using a population database. *Arch Dis Child*
1010 **88**:38–43. doi:10.1136/adc.88.1.38
1011 Cronk JC, Derecki NC, Ji E, Xu Y, Lampano AE, Smirnov I, Baker W, Norris GT, Marin I, Coddington N, Wolf
1012 Y, Turner SD, Aderem A, Klibanov AL, Harris TH, Jung S, Litvak V, Kipnis J. 2015. Methyl-CpG
1013 Binding Protein 2 Regulates Microglia and Macrophage Gene Expression in Response to
1014 Inflammatory Stimuli. *Immunity* **42**:679–691. doi:10.1016/j.immuni.2015.03.013
1015 De Felice C, Signorini C, Leoncini S, Pecorelli A, Durand T, Valacchi G, Ciccoli L, Hayek J. 2012. The role of
1016 oxidative stress in Rett syndrome: an overview. *Ann N Y Acad Sci* **1259**:121–135.
1017 doi:10.1111/j.1749-6632.2012.06611.x
1018 Dellu F, Contarino A, Simon H, Koob GF, Gold LH. 2000. Genetic Differences in Response to Novelty and
1019 Spatial Memory Using a Two-Trial Recognition Task in Mice. *Neurobiol Learn Mem* **73**:31–48.
1020 doi:10.1006/nlme.1999.3919
1021 Derecki NC, Cronk JC, Lu Z, Xu E, Abbott SBG, Guyenet PG, Kipnis J. 2012. Wild-type microglia arrest
1022 pathology in a mouse model of Rett syndrome. *Nature* **484**:105–109. doi:10.1038/nature10907
1023 Ding Q, Wu X, Li X, Wang H. 2021. Vorinostat Corrects Cognitive and Non-Cognitive Symptoms in a
1024 Mouse Model of Fragile X Syndrome. *Int J Neuropsychopharmacol* pyab081.
1025 doi:10.1093/ijnp/pyab081
1026 Downs J, Géranton SM, Bebbington A, Jacoby P, Bahi-Buisson N, Ravine D, Leonard H. 2010. Linking
1027 MECP2 and pain sensitivity: The example of Rett syndrome. *Am J Med Genet A* **152A**:1197–1205.
1028 doi:10.1002/ajmg.a.33314

1029 Exner CRT, Willsey HR. 2021. Xenopus leads the way: Frogs as a pioneering model to understand the
1030 human brain. *genesis* **59**:e23405. doi:10.1002/dvg.23405
1031 Forbes M. 2021. py-factorgraph.
1032 Franken H, Mathieson T, Childs D, Sweetman GMA, Werner T, Tögel I, Doce C, Gade S, Bantscheff M,
1033 Drewes G, Reinhard FBM, Huber W, Savitski MM. 2015. Thermal proteome profiling for
1034 unbiased identification of direct and indirect drug targets using multiplexed quantitative mass
1035 spectrometry. *Nat Protoc* **10**:1567–1593. doi:10.1038/nprot.2015.101
1036 Gabel HW, Kinde B, Stroud H, Gilbert CS, Harmin DA, Kastan NR, Hemberg M, Ebert DH, Greenberg ME.
1037 2015. Disruption of DNA-methylation-dependent long gene repression in Rett syndrome. *Nature*
1038 **522**:89–93. doi:10.1038/nature14319
1039 Gaetani M, Sabatier P, Saei AA, Beusch CM, Yang Z, Lundström SL, Zubarev RA. 2019. Proteome Integral
1040 Solubility Alteration: A High-Throughput Proteomics Assay for Target Deconvolution. *J Proteome*
1041 *Res* **18**:4027–4037. doi:10.1021/acs.jproteome.9b00500
1042 Giacometti E, Luikenhuis S, Beard C, Jaenisch R. 2007. Partial rescue of MeCP2 deficiency by postnatal
1043 activation of MeCP2. *Proc Natl Acad Sci* **104**:1931–1936. doi:10.1073/pnas.0610593104
1044 Glaze DG, Neul JL, Percy A, Feyma T, Beisang A, Yaroshinsky A, Stoms G, Zuchero D, Horrigan J, Glass L,
1045 Jones NE. 2017. A Double-Blind, Randomized, Placebo-Controlled Clinical Study of Trofinetide in
1046 the Treatment of Rett Syndrome. *Pediatr Neurol* **76**:37–46.
1047 doi:10.1016/j.pediatrneurol.2017.07.002
1048 Gold WA, Lacina TA, Cantrill LC, Christodoulou J. 2015. MeCP2 deficiency is associated with reduced
1049 levels of tubulin acetylation and can be restored using HDAC6 inhibitors. *J Mol Med Berl Ger*
1050 **93**:63–72. doi:10.1007/s00109-014-1202-x
1051 Guy J, Gan J, Selfridge J, Cobb S, Bird A. 2007. Reversal of Neurological Defects in a Mouse Model of Rett
1052 Syndrome. *Science* **315**:1143–1147. doi:10.1126/science.1138389

1053 Guy J, Hendrich B, Holmes M, Martin JE, Bird A. 2001. A mouse *Mecp2*-null mutation causes neurological
1054 symptoms that mimic Rett syndrome. *Nat Genet* **27**:322–326. doi:10.1038/85899
1055 Hagberg B. 2002. Clinical manifestations and stages of rett syndrome. *Ment Retard Dev Disabil Res Rev*
1056 **8**:61–65. doi:10.1002/mrdd.10020
1057 Han H, Cho J-W, Lee Sangyoung, Yun A, Kim H, Bae D, Yang S, Kim CY, Lee M, Kim E, Lee Sungho, Kang B,
1058 Jeong D, Kim Y, Jeon H-N, Jung H, Nam S, Chung M, Kim J-H, Lee I. 2018. TRRUST v2: an
1059 expanded reference database of human and mouse transcriptional regulatory interactions.
1060 *Nucleic Acids Res* **46**:D380–D386. doi:10.1093/nar/gkx1013
1061 Hewapathirane DS, Dunfield D, Yen W, Chen S, Haas K. 2008. In vivo imaging of seizure activity in a novel
1062 developmental seizure model. *Exp Neurol* **211**:480–488. doi:10.1016/j.expneurol.2008.02.012
1063 Hockly E, Richon VM, Woodman B, Smith DL, Zhou X, Rosa E, Sathasivam K, Ghazi-Noori S, Mahal A,
1064 Lowden PAS, Steffan JS, Marsh JL, Thompson LM, Lewis CM, Marks PA, Bates GP. 2003.
1065 Suberoylanilide hydroxamic acid, a histone deacetylase inhibitor, ameliorates motor deficits in a
1066 mouse model of Huntington's disease. *Proc Natl Acad Sci U S A* **100**:2041–2046.
1067 doi:10.1073/pnas.0437870100
1068 Huber KVM, Olek KM, Müller AC, Tan CSH, Bennett KL, Colinge J, Superti-Furga G. 2015. Proteome-wide
1069 drug and metabolite interaction mapping by thermal-stability profiling. *Nat Methods* **12**:1055–
1070 1057. doi:10.1038/nmeth.3590
1071 Huynh-Thu VA, Irrthum A, Wehenkel L, Geurts P. 2010. Inferring Regulatory Networks from Expression
1072 Data Using Tree-Based Methods. *PLOS ONE* **5**:e12776. doi:10.1371/journal.pone.0012776
1073 Kanehisa M, Goto S. 2000. KEGG: kyoto encyclopedia of genes and genomes. *Nucleic Acids Res* **28**:27–
1074 30.
1075 Kerr AM, Nomura Y, Armstrong D, Anvret M, Belichenko PV, Budden S, Cass H, Christodoulou J, Clarke A,
1076 Ellaway C, d'Esposito M, Francke U, Hulten M, Julu P, Leonard H, Naidu S, Schanen C, Webb T,

1077 Engerstrom IW, Yamashita Y, Segawa M. 2001. Guidelines for reporting clinical features in cases
1078 with MECP2 mutations. *Brain Dev* **23**:208–211. doi:10.1016/S0387-7604(01)00193-0
1079 Kulkarni SS, Griffin JN, Date PP, Liem KF, Khokha MK. 2018. WDR5 Stabilizes Actin Architecture to
1080 Promote Multiciliated Cell Formation. *Dev Cell* **46**:595-610.e3. doi:10.1016/j.devcel.2018.08.009
1081 Labun K, Montague TG, Gagnon JA, Thyme SB, Valen E. 2016. CHOPCHOP v2: a web tool for the next
1082 generation of CRISPR genome engineering. *Nucleic Acids Res* **44**:W272-276.
1083 doi:10.1093/nar/gkw398
1084 Lamb J, Crawford ED, Peck D, Modell JW, Blat IC, Wrobel MJ, Lerner J, Brunet J-P, Subramanian A, Ross
1085 KN, Reich M, Hieronymus H, Wei G, Armstrong SA, Haggarty SJ, Clemons PA, Wei R, Carr SA,
1086 Lander ES, Golub TR. 2006. The Connectivity Map: using gene-expression signatures to connect
1087 small molecules, genes, and disease. *Science* **313**:1929–1935. doi:10.1126/science.1132939
1088 Lebrun N, Delépine C, Selloum M, Meziane H, Nectoux J, Herault Y, Bienvenu T. 2021. HDAC inhibitor
1089 ameliorates behavioral deficits in Mecp2308/y mouse model of Rett syndrome. *Brain Res*
1090 147670. doi:10.1016/j.brainres.2021.147670
1091 Li W, Pozzo-Miller L. 2014. BDNF deregulation in Rett syndrome. *Neuropharmacology*, BDNF Regulation
1092 of Synaptic Structure, Function, and Plasticity **76**:737–746.
1093 doi:10.1016/j.neuropharm.2013.03.024
1094 Lonowski LA, Narimatsu Y, Riaz A, Delay CE, Yang Z, Niola F, Duda K, Ober EA, Clausen H, Wandall HH,
1095 Hansen SH, Bennett EP, Frödin M. 2017. Genome editing using FACS enrichment of nuclease-
1096 expressing cells and indel detection by amplicon analysis. *Nat Protoc* **12**:581–603.
1097 doi:10.1038/nprot.2016.165
1098 Luikenhuis S, Giacometti E, Beard CF, Jaenisch R. 2004. Expression of MeCP2 in postmitotic neurons
1099 rescues Rett syndrome in mice. *Proc Natl Acad Sci U S A* **101**:6033–6038.
1100 doi:10.1073/pnas.0401626101

1101 Martínez de Paz A, Sanchez-Mut JV, Samitier-Martí M, Petazzi P, Sáez M, Szczesna K, Huertas D, Esteller
1102 M, Ausió J. 2015. Circadian Cycle-Dependent MeCP2 and Brain Chromatin Changes. *PLoS ONE*
1103 **10**. doi:10.1371/journal.pone.0123693
1104 Mateus A, Määttä TA, Savitski MM. 2017. Thermal proteome profiling: unbiased assessment of protein
1105 state through heat-induced stability changes. *Proteome Sci* **15**:13. doi:10.1186/s12953-017-
1106 0122-4
1107 Miller RA, Ehrhart F, Eijssen LMT, Slenter DN, Curfs LMG, Evelo CT, Willighagen EL, Kutmon M. 2019.
1108 Beyond Pathway Analysis: Identification of Active Subnetworks in Rett Syndrome. *Front Genet*
1109 **10**:59. doi:10.3389/fgene.2019.00059
1110 Morton J, Snider TA. 2017. Guidelines for collection and processing of lungs from aged mice for
1111 histological studies. *Pathobiol Aging Age-Relat Dis* **7**:1313676.
1112 doi:10.1080/20010001.2017.1313676
1113 Motil KJ, Caeg E, Barrish JO, Geerts S, Lane JB, Percy AK, Annese F, McNair L, Skinner SA, Lee H-S, Neul JL,
1114 Glaze DG. 2012. Gastrointestinal and nutritional problems occur frequently throughout life in
1115 girls and women with Rett syndrome. *J Pediatr Gastroenterol Nutr* **55**:292–298.
1116 doi:10.1097/MPG.0b013e31824b6159
1117 Nalle SC, Zuo L, Ong MLDM, Singh G, Worthylake AM, Choi W, Manresa MC, Southworth AP, Edelblum
1118 KL, Baker GJ, Joseph NE, Savage PA, Turner JR. 2019. Graft-versus-host disease propagation
1119 depends on increased intestinal epithelial tight junction permeability. *J Clin Invest* **129**:902–914.
1120 doi:10.1172/JCI98554
1121 Nenni MJ, Fisher ME, James-Zorn C, Pells TJ, Ponferrada V, Chu S, Fortriede JD, Burns KA, Wang Y, Lotay
1122 VS, Wang DZ, Segerdell E, Chaturvedi P, Karimi K, Vize PD, Zorn AM. 2019. Xenbase: Facilitating
1123 the Use of Xenopus to Model Human Disease. *Front Physiol* **10**. doi:10.3389/fphys.2019.00154
1124 NIH LINCS Program. n.d. https://lincsproject.org/

1125 O'Driscoll CM, Lima MP, Kaufmann WE, Bressler JP. 2015. Methyl CpG binding protein 2 deficiency
1126 enhances expression of inflammatory cytokines by sustaining NF-κB signaling in myeloid derived
1127 cells. *J Neuroimmunol* **283**:23–29. doi:10.1016/j.jneuroim.2015.04.005
1128 Pearl J. 1982. Reverend bayes on inference engines: a distributed hierarchical approachProceedings of
1129 the Second AAAI Conference on Artificial Intelligence, AAAI'82. Pittsburgh, Pennsylvania: AAAI
1130 Press. pp. 133–136.
1131 Potts EM, Coppotelli G, Ross JM. 2020. Histological-Based Stainings using Free-Floating Tissue Sections. *J*
1132 *Vis Exp JoVE*. doi:10.3791/61622
1133 Pratt KG, Khakhalin AS. 2013. Modeling human neurodevelopmental disorders in the Xenopus tadpole:
1134 from mechanisms to therapeutic targets. *Dis Model Mech* **6**:1057–1065.
1135 doi:10.1242/dmm.012138
1136 Przanowski P, Wasko U, Zheng Z, Yu J, Sherman R, Zhu LJ, McConnell MJ, Tushir-Singh J, Green MR,
1137 Bhatnagar S. 2018. Pharmacological reactivation of inactive X-linked Mecp2 in cerebral cortical
1138 neurons of living mice. *Proc Natl Acad Sci* **115**:7991–7996. doi:10.1073/pnas.1803792115
1139 Renthal W, Boxer LD, Hrvatin S, Li E, Silberfeld A, Nagy MA, Griffith EC, Vierbuchen T, Greenberg ME.
1140 2018. Characterization of human mosaic Rett syndrome brain tissue by single-nucleus RNA
1141 sequencing. *Nat Neurosci* **21**:1670–1679. doi:10.1038/s41593-018-0270-6
1142 Russo PST, Ferreira GR, Cardozo LE, Bürger MC, Arias-Carrasco R, Maruyama SR, Hirata TDC, Lima DS,
1143 Passos FM, Fukutani KF, Lever M, Silva JS, Maracaja-Coutinho V, Nakaya HI. 2018. CEMiTool: a
1144 Bioconductor package for performing comprehensive modular co-expression analyses. *BMC*
1145 *Bioinformatics* **19**:56. doi:10.1186/s12859-018-2053-1
1146 Ruthsatz K, Dausmann KH, Peck MA, Drees C, Sabatino NM, Becker LI, Reese J, Hartmann L, Glos J. 2018.
1147 Thyroid hormone levels and temperature during development alter thermal tolerance and
1148 energetics of Xenopus laevis larvae. *Conserv Physiol* **6**. doi:10.1093/conphys/coy059

1149 Sanfeliu A, Hokamp K, Gill M, Tropea D. 2019. Transcriptomic Analysis of Mecp2 Mutant Mice Reveals
1150 Differentially Expressed Genes and Altered Mechanisms in Both Blood and Brain. *Front*
1151 *Psychiatry* **10**:278. doi:10.3389/fpsyt.2019.00278
1152 Schafer DP, Heller CT, Gunner G, Heller M, Gordon C, Hammond T, Wolf Y, Jung S, Stevens B. 2016.
1153 Microglia contribute to circuit defects in Mecp2 null mice independent of microglia-specific loss
1154 of Mecp2 expression. *eLife* **5**:e15224. doi:10.7554/eLife.15224
1155 Sekhon RS, Briskine R, Hirsch CN, Myers CL, Springer NM, Buell CR, de Leon N, Kaeppler SM. 2013. Maize
1156 gene atlas developed by RNA sequencing and comparative evaluation of transcriptomes based
1157 on RNA sequencing and microarrays. *PloS One* **8**:e61005. doi:10.1371/journal.pone.0061005
1158 Subramanian A, Narayan R, Corsello SM, Peck DD, Natoli TE, Lu X, Gould J, Davis JF, Tubelli AA, Asiedu JK,
1159 Lahr DL, Hirschman JE, Liu Z, Donahue M, Julian B, Khan M, Wadden D, Smith IC, Lam D, Liberzon
1160 A, Toder C, Bagul M, Orzechowski M, Enache OM, Piccioni F, Johnson SA, Lyons NJ, Berger AH,
1161 Shamji AF, Brooks AN, Vrcic A, Flynn C, Rosains J, Takeda DY, Hu R, Davison D, Lamb J, Ardlie K,
1162 Hogstrom L, Greenside P, Gray NS, Clemons PA, Silver S, Wu Xiaoyun, Zhao W-N, Read-Button
1163 W, Wu Xiaohua, Haggarty SJ, Ronco LV, Boehm JS, Schreiber SL, Doench JG, Bittker JA, Root DE,
1164 Wong B, Golub TR. 2017. A Next Generation Connectivity Map: L1000 Platform and the First
1165 1,000,000 Profiles. *Cell* **171**:1437-1452.e17. doi:10.1016/j.cell.2017.10.049
1166 Szczesna K, de la Caridad O, Petazzi P, Soler M, Roa L, Saez MA, Fourcade S, Pujol A, Artuch-Iriberri R,
1167 Molero-Luis M, Vidal A, Huertas D, Esteller M. 2014. Improvement of the Rett Syndrome
1168 Phenotype in a Mecp2 Mouse Model Upon Treatment with Levodopa and a Dopa-Decarboxylase
1169 Inhibitor. *Neuropsychopharmacology* **39**:2846–2856. doi:10.1038/npp.2014.136
1170 Tarquinio DC, Hou W, Neul JL, Lane JB, Barnes KV, O'Leary HM, Bruck NM, Kaufmann WE, Motil KJ, Glaze
1171 DG, Skinner SA, Annese F, Baggett L, Barrish JO, Geerts SP, Percy AK. 2015. Age of diagnosis in

1172 Rett syndrome: patterns of recognition among diagnosticians and risk factors for late diagnosis.
1173 *Pediatr Neurol* **52**:585-591.e2. doi:10.1016/j.pediatrneurol.2015.02.007
1174 The Comparative Toxicogenomics Database | CTD. n.d. http://ctdbase.org/
1175 Timmerman R, Burm SM, Bajramovic JJ. 2018. An Overview of in vitro Methods to Study Microglia. *Front*
1176 *Cell Neurosci* **12**. doi:10.3389/fncel.2018.00242
1177 Tsai P-Y, Zhang B, He W-Q, Zha J-M, Odenwald MA, Singh G, Tamura A, Shen L, Sailer A, Yeruva S, Kuo W-
1178 T, Fu Y-X, Tsukita S, Turner JR. 2017. IL-22 Upregulates Epithelial Claudin-2 to Drive Diarrhea and
1179 Enteric Pathogen Clearance. *Cell Host Microbe* **21**:671-681.e4. doi:10.1016/j.chom.2017.05.009
1180 Varderidou-Minasian S, Hinz L, Hagemans D, Posthuma D, Altelaar M, Heine VM. 2020. Quantitative
1181 proteomic analysis of Rett iPSC-derived neuronal progenitors. *Mol Autism* **11**:38.
1182 doi:10.1186/s13229-020-00344-3
1183 Vashi N, Justice MJ. 2019. Treating Rett syndrome: from mouse models to human therapies. *Mamm*
1184 *Genome*. doi:10.1007/s00335-019-09793-5
1185 Willsey HR. 2021. Whole-Mount RNA In Situ Hybridization and Immunofluorescence of Xenopus
1186 Embryos and Tadpoles. *Cold Spring Harb Protoc* **2021**:pdb.prot105635.
1187 doi:10.1101/pdb.prot105635
1188 Yang Z, Steentoft C, Hauge C, Hansen L, Thomsen AL, Niola F, Vester-Christensen MB, Frödin M, Clausen
1189 H, Wandall HH, Bennett EP. 2015. Fast and sensitive detection of indels induced by precise gene
1190 targeting. *Nucleic Acids Res* **43**:e59. doi:10.1093/nar/gkv126
1191